Journal of Rock Mechanics and Geotechnical Engineering 14 (2022) 180–196

Contents lists available at ScienceDirect

Journal of Rock Mechanics and Geotechnical Engineering

journal homepage: www.jrmge.cn

Full Length Article

The use of the node-based smoothed finite element method to estimate static and seismic bearing capacities of shallow strip footings

H.C. Nguyen [a,b,*], T. Vo-Minh [c]

[a] Department of Civil and Environmental Engineering, Imperial College London, UK
[b] Department of Civil Engineering and Industrial Design, University of Liverpool, Liverpool, UK
[c] Faculty of Civil Engineering, Ho Chi Minh City University of Technology (HUTECH), Ho Chi Minh City, Viet Nam

ARTICLE INFO

Article history:
Received 3 June 2021
Received in revised form
19 September 2021
Accepted 21 November 2021
Available online 16 December 2021

Keywords:
Limit analysis
Node-based smoothed finite element method (NS-FEM)
Second-order cone programming (SOCP)
Seismic bearing capacity
Strip footing

ABSTRACT

The node-based smoothed finite element method (NS-FEM) is shortly presented for calculations of the static and seismic bearing capacities of shallow strip footings. A series of computations has been performed to assess variations in seismic bearing capacity factors with both horizontal and vertical seismic accelerations. Numerical results obtained agree very well with those using the slip-line method, revealing that the magnitude of the seismic bearing capacity is highly dependent upon the combinations of various directions of both components of the seismic acceleration. An upward vertical seismic acceleration reduces the seismic bearing capacity compared to the downward vertical seismic acceleration in calculations. In addition, particular emphasis is placed on a separate estimation of the effects of soil and superstructure inertia on each seismic bearing capacity component. While the effect of inertia forces arising in the soil on the seismic bearing capacity is non-trivial, and the superstructure inertia is the major contributor to reductions in the seismic bearing capacity. Both tables and charts are given for practical application to the seismic design of the foundations.

1. Introduction

The bearing capacity of strip footings under static conditions has been extensively studied by Prandtl (1920), Terzaghi (1943), Meyerhof (1951), Hansen (1970), Vesic (1973), and many others. In recent years, the effect of horizontal earthquake body forces on shallow foundation bearing capacity is an important topic of research in geotechnical engineering. The first studies were describing the seismic bearing capacity of shallow foundations concerning the works of Meyerhof (1953, 1963), where the seismic forces were applied at the structure only as inclined pseudo-static loads. However, in these solutions, the inertia of the soil mass is not included. In the presence of seismic forces, the available theoretical researches are mainly based on (i) the limit equilibrium method; (ii) the upper and lower bound limit analysis; and (iii) the method of stress characteristics (slip-line method).

Using the limit equilibrium method, Sarma and Iossifelis (1990) determined the seismic bearing capacity of strip footings considering the failure mechanisms of three zones as the unsymmetrical active wedge, internal shear zone and passive wedge. Later on, Budhu and Al-Karni (1993) investigated an asymmetrical failure surface for seismic analysis of shallow foundations with similar three zones as that Vesic (1973) considered. Choudhury and Subba Rao (2005) considered two mechanisms, log-spiral curve, and planar active wedge and passive wedge, to calculate the seismic force on the structure and soil below. Recently, Saha and Ghosh (2015) investigated the seismic bearing capacity of strip footings using pseudo-dynamic coupled with the limit equilibrium method.

Based on the upper bound theorem, Richards et al. (1993) used two triangular planar wedges in the failure surface, each on the active and passive zones, to investigate the effect of soil and superstructure inertia on the seismic bearing capacity of strip footings. Dormieux and Pecker (1995) and Soubra (1999) investigated the seismic bearing capacity of strip foundation on the horizontal using pseudo-static method. Ghosh (2008) and Saha et al. (2018) used a pseudo-dynamic approach to explore the effect of shear and primary wave velocities and amplification factor on the seismic bearing capacity of strip footings using the upper bound limit

* Corresponding author. Department of Civil and Environmental Engineering, Imperial College London, UK.
E-mail addresses: h.nguyen15@imperial.ac.uk, H.C.Nguyen@liverpool.ac.uk (H.C. Nguyen).

Peer review under responsibility of Institute of Rock and Soil Mechanics, Chinese Academy of Sciences.

https://doi.org/10.1016/j.jrmge.2021.11.005

analysis. More recently, Kalouzari et al. (2019) investigated the seismic bearing capacity of strip foundations in the vicinity of slopes using the lower bound finite element method (FEM) in conjunction with the linear programming technique.

Using the method of characteristics, Kumar and Mohan Rao (2003) and Kumar (2003) presented the variation of the seismic bearing capacity with changes in horizontal seismic coefficients for different slope inclinations. Although seismic bearing factors reduce as the horizontal seismic acceleration increases, the evolution of characteristics line networks depends on soil and superstructure inertia in a complex manner. Recently, Cascone and Casablanca (2016) used the method of characteristics to compute the bearing capacity factors of strip footings and evolutions of failure patterns with the horizontal seismic acceleration for each seismic case. The effects of the soil inertia force and the superstructure inertia with variation in horizontal seismic coefficients are distinguished in the analysis.

In recent decades, the FEM plays an important role in designing many practical engineering structural systems. Due to the simplicity, the 3-node linear triangular elements (FEM-T3) are popular. One of the notable drawbacks of FEM-T3 elements is the volumetric locking phenomenon when the mesh becomes highly distorted. In the standard FEM, the stiffness matrix is used to map basis function derivatives from the reference element to the natural element in the mesh. When distorted meshes are used in the FEM, the Jacobian becomes ill-conditioned, affecting the accuracy of the method.

To overcome this, Liu et al. (2007a, b, 2009a, b) have combined the strain smoothing technique used in meshfree methods (Chen et al., 2001) into the FEM to formulate a series of smoothed FEMs used in the field of solid mechanics. The basic idea of strain smoothing based on the domain integration on the cells becomes line integration along the boundary of the cell. In the node-based smoothed FEM (NS-FEM), the strain smoothing technique over the cells associated with nodes is computed directly using only the shape functions themselves (not their derivatives), which eliminates the volumetric locking phenomenon. As a result, no coordinate transformation is required in the NS-FEM, and the problem domain can be discretized in highly distorted meshes. NS-FEM has been successfully applied to several fields, including structural mechanics, solid mechanics, acoustic analysis, and electromagnetic problems.

Together with NS-FEM, other smoothed FEM have been applied to computation of the collapse loads; and numerical results reveal that the smoothed FEMs are naturally “immune” from the volumetric locking. In particular, Le et al. (2010) presented an upper bound procedure using cell-based smoothed FEM, arriving at conclusions that the use of the strain smoothing technique can overcome the volumetric locking and provide accurate results of the collapse loads with minimal computational effort. In addition, Nguyen-Xuan et al. (2012) stated that combination of the node-based FEM and primal-dual algorithm serves as a better means of calculating the limit and shakedown loads of structures when compared with the available solutions. Application of the smoothing technique over the edge of triangle elements to the kinematic limit analysis was presented by Le et al. (2013), in which the volume locking is removed for the plane stress and strain problems when using only one Gauss point for each smoothing domain. More recently, the cell-based smoothed FEM is applied to limit and shakedown analyses of structures (Ho et al., 2019) and the collapse of soil (Le, 2017).

Recently, the application of the smoothed FEM to the upper bound limit analysis in geotechnical problems has been developed by Nguyen et al. (2011), Nguyen (2020, 2021a, b), Vo-Minh et al. (2017, 2018), Vo-Minh (2020), Vo-Minh and Nguyen-Son (2021), and Nguyen and Vo-Minh (2022). The Mohr-Coulomb yield criterion can be formed in a second-order cone programming (SOCP) using the NS-FEM in geomechanics problems. The problem can then be solved by the primal-dual interior-point method implemented in the MOSEK software package (MOSEK ApS, 2009). This algorithm was proved to be a very effective optimization tool for limit analysis in geotechnical engineering. In order to assess the effects of the earthquake on the stability, the so-called pseudo-static approach has been widely used because of its simplicity to be implemented in the numerical procedure and its ability to produce acceptable solutions to plasticity problems in geotechnical engineering under seismic conditions (Ausilio et al., 2000; Sahoo and Kumar, 2012, 2014; Chakraborty and Kumar, 2013; Krabbenhoft, 2018). Seismic effects on the bearing capacity are represented by considering relevant inertia forces which are proportional to seismic accelerations in both the vertical and horizontal directions. Installing these forces in the simulations is straightforward as noted in Ausilio et al. (2000), Sahoo and Kumar (2012, 2014), Chakraborty and Kumar (2013) and Krabbenhoft (2018), and is further discussed in the following section for each seismic bearing capacity problem. The dynamic problems turn now to solve the standard static problems which are augmented by inertial forces due to the soil weight, surcharge and the structure.

It is considered important that the effects of cyclic loads cannot be explored using limit analysis, thus the shakedown analysis (Nguyen-Xuan et al., 2012) or the dynamic analysis (Wang et al., 2021a, b) should be performed to further understand the bearing capacity of soils under cyclic loads. One of the main features of soil under cyclic loading is the accumulation of strain or deformation during a great number of cycles that result in significant reduction of behaviors (Abadie, 2015; Houlsby et al., 2017; Abadie et al., 2019). Under cyclic loads and seismic forces, due to rapid changes in shaking direction and amplitude during earthquake, the available soil shear strength under a foundation may repeatedly and momentarily be attained, inducing several instantaneous failures. In addition, due to the reduction of footing–soil contact area, the accumulated permanent rotation of the foundation reduces the bearing capacity of strip footings. The seismic loads can be represented by pseudo-static loads using corrective parameters, which are further discussed in the analysis by changing the direction of seismic acceleration.

In this paper, we present the upper bound limit analysis using the NS-FEM to estimate the seismic bearing capacity factors of strip footings based on the pseudo-static approach. In general, increasing the horizontal seismic acceleration of inertia force and superstructure inertia reduces the seismic bearing capacity factors of strip footings. The corrective coefficients are presented to point out the reduction in the seismic bearing capacity factors due to the effects of soil and superstructure inertia. The numerical results obtained by the NS-FEM are compared with those from Cascone and Casablanca (2016) and previous studies to verify the proposed method’s accuracy and reliability.

The paper is arranged as follows. Section 2 describes a brief review of the NS-FEM for the upper bound limit analysis in the geomechanical problems. In Section 3, several numerical examples are performed and discussed to demonstrate the effectiveness of the NS-FEM. Finally, some concluding remarks are made in Section 4.

2. The NS-FEM for upper bound limit analysis of the geomechanical problems

2.1. A brief overview of the NS-FEM

Unlike the traditional FEM, the numerical integration domains of the NS-FEM are based on polygonal cells related to the nodes

rather than the elements. The problem domain Ω is divided into N_s smoothing cells formulated as $\Omega = \sum_{k=1}^{N_s} \Omega_k^s$ and $\Omega_i^s \cap \Omega_j^s = \varnothing$ ($i \neq j$), where N_s is the total number of field nodes in the entire problem domain. The polygonal cell, Ω_k^s, called a nodal smoothing domain associated with the node k, is constructed by connecting the mid-edge points sequentially to the centroid of surrounding triangular elements, as shown in Fig. 1. The smoothing domain boundary Ω_k^s is labeled as Γ_k, and the union of all Ω_k^s forms precisely the whole problem Ω.

The smoothed strain on the cell Ω_k^s associated with the node k using the NS-FEM can be calculated by

$$\tilde{\dot{\boldsymbol{\varepsilon}}}_k = \sum_{k \in \boldsymbol{N}^{(s)}} \tilde{\boldsymbol{B}}_k(x_s)\boldsymbol{d}_k \tag{1}$$

where $\boldsymbol{N}^{(s)}$ is the set containing nodes directly connected to node k, $\boldsymbol{d}_k$ is the nodal displacement vector, and the smoothed strain gradient matrix $\tilde{\boldsymbol{B}}_k(x_s)$ on the domain Ω_k^s can be determined as

$$\tilde{\boldsymbol{B}}_k(x_s) = \begin{bmatrix} \tilde{b}_{kx}(x_s) & 0 \\ 0 & \tilde{b}_{ky}(x_s) \\ \tilde{b}_{ky}(x_s) & \tilde{b}_{kx}(x_s) \end{bmatrix} \tag{2}$$

$$\tilde{b}_{kh}(x_s) = \frac{1}{A_k^{(s)}} \int_{\Gamma_k} \boldsymbol{n}_h^{(s)}(x) N_k(x)\, \mathrm{d}\Gamma \quad (h = x, y) \tag{3}$$

where $A_k^{(s)} = \int_{\Omega_k^s} \mathrm{d}\Omega$ is the area of the cell Ω_k^s, $N_k(x)$ is the FEM shape function for the node k, and $\boldsymbol{n}^{(s)}(x)$ is the normal outward vector on the boundary $\Gamma_k^{(s)}$. The number of Gauss points for line integration (Eq. (3)) depends on the degree of N_k. If N_k is a linear shape function, one Gauss point is sufficient for line integration along each segment of the boundary $\Gamma_k^{(s)}$ of Ω_k^s, Eq. (3) can be transformed to its algebraic form:

$$\tilde{b}_{kh}(x_s) = \frac{1}{A_k^{(s)}} \sum_{k=1}^{M} \boldsymbol{N}_k\left(x_k^{GP}\right) \boldsymbol{n}_{kh}^{(s)} l_k^{(s)} \quad (h = x, y) \tag{4}$$

where M is the total number of the boundary segment $\Gamma_k^{(s)}$; and x_k^{GP} is the Gauss point of the boundary segment $\Gamma_k^{(s)}$, which has length $l_k^{(s)}$ and outward unit normal $\boldsymbol{n}_{kh}^{(s)}$.

2.2. The upper bound limit analysis for plane strain geotechnical problems using the NS-FEM

A two-dimensional (2D) problem domain Ω bounded by a continuous boundary $S_{\boldsymbol{u}} \cup S_{\boldsymbol{t}} = S$ and $S_{\boldsymbol{u}} \cap S_{\boldsymbol{t}} = \varnothing$ is considered. The rigid-perfectly plastic body is subjected to external traction load $\boldsymbol{g}$ on S_t and body force $\boldsymbol{f}$ on the boundary $S_{\boldsymbol{u}}$ prescribed by the displacement velocity vector $\dot{\boldsymbol{u}}$. The strain rate can be expressed by

$$\dot{\boldsymbol{\varepsilon}} = \begin{bmatrix} \dot{\varepsilon}_{xx} & \dot{\varepsilon}_{yy} & \dot{\gamma}_{xy} \end{bmatrix}^{\mathrm{T}} = \nabla \dot{\boldsymbol{u}} \tag{5}$$

In the upper bound theorem, for a kinematically admissible displacement field $\dot{\boldsymbol{u}} \in \boldsymbol{U}$, where $\boldsymbol{U}$ is a space of kinematically admissible velocity field, we have

$$W_{\mathrm{int}}(\boldsymbol{\sigma}, \dot{\boldsymbol{u}}) = \alpha^{+} W_{\mathrm{ext}}(\dot{\boldsymbol{u}}) \tag{6}$$

where α^{+} is the limit load multiplier of the external traction load $\boldsymbol{g}$ and body force $\boldsymbol{f}$.

The external work can be determined as

$$W_{\mathrm{ext}}(\dot{\boldsymbol{u}}) = \int_{\Omega} \boldsymbol{f}\dot{\boldsymbol{u}}\mathrm{d}\Omega + \int_{\Gamma_t} \boldsymbol{g}\dot{\boldsymbol{u}}\mathrm{d}S \tag{7}$$

The internal plastic dissipation of the 2D domain Ω can be written as

$$W_{\mathrm{int}}(\boldsymbol{\sigma}, \dot{\boldsymbol{u}}) = \int_{\Omega} D_{\mathrm{p}}(\dot{\boldsymbol{u}})\mathrm{d}\Omega = \int_{\Omega} \boldsymbol{\sigma}\dot{\boldsymbol{\varepsilon}}\mathrm{d}\Omega \tag{8}$$

in which the space of kinematically admissible velocity field $\boldsymbol{U}$ is denoted by

$$\boldsymbol{U} = \left\{ \dot{\boldsymbol{u}} \in \left(H^1(\Omega)\right)^2,\ \dot{\boldsymbol{u}} = \bar{\dot{\boldsymbol{u}}} \text{ on } S_{\dot{\boldsymbol{u}}} \right\} \tag{9}$$

Defining $\boldsymbol{C} = \{\dot{\boldsymbol{u}} \in \boldsymbol{U} | W_{\mathrm{ext}}(\dot{\boldsymbol{u}}) = 1\}$, the limit analysis problem is based on the kinematical theorem to determine the collapse multiplier α^{+} yielding the following optimization problem:

$$\alpha^{+} = \max\left\{ \exists \boldsymbol{\sigma} \in \sum | W_{\mathrm{int}}(\boldsymbol{\sigma}, \dot{\boldsymbol{u}}) = \alpha W_{\mathrm{ext}}(\dot{\boldsymbol{u}}), \forall \dot{\boldsymbol{u}} \in \boldsymbol{U} \right\} = \min_{\dot{\boldsymbol{u}} \in \boldsymbol{U}} D_{\mathrm{p}}(\dot{\boldsymbol{u}})$$
$$(\dot{\boldsymbol{u}} = 0\ (\text{on } S_{\boldsymbol{u}}),\ W_{\mathrm{ext}}(\dot{\boldsymbol{u}}) = 1) \tag{10}$$

For plane strain geotechnical problems, Makrodimopoulos and Martin (2007) proposed the internal plastic dissipation equation as follows:

$$D_{\mathrm{p}}(\dot{\boldsymbol{u}}) = c \cos\phi \int_{\Omega} \sqrt{\left(\tilde{\dot{\varepsilon}}_{xx}^{i} - \tilde{\dot{\varepsilon}}_{yy}^{i}\right)^2 + \left(\tilde{\dot{\gamma}}_{xy}^{i}\right)^2} \mathrm{d}\Omega \tag{11}$$

where c and ϕ are the cohesion and friction angle of the soil, respectively.

For an associated flow rule, the plastic strain rate vector is given by

$$\dot{\boldsymbol{\varepsilon}} = \mu \frac{\partial \psi(\boldsymbol{\sigma})}{\partial \boldsymbol{\sigma}} \tag{12}$$

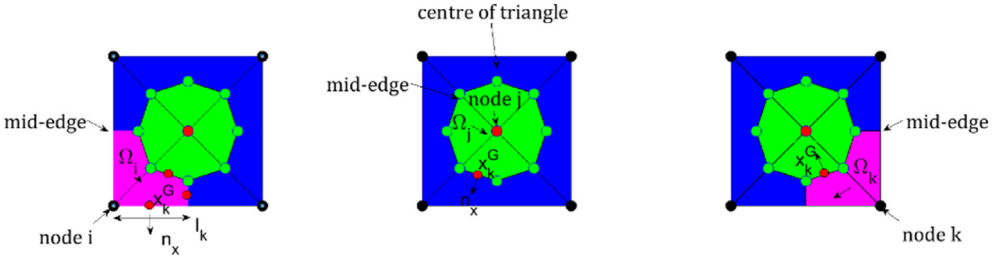

Fig. 1. The smoothing cells associated with the nodes in the NS-FEM.

where μ is a non-negative plastic multiplier, and the Mohr–Coulomb yield function $\psi(\boldsymbol{\sigma})$ can be expressed in the form of stress components as

$$\psi(\boldsymbol{\sigma}) = \sqrt{(\sigma_{xx}-\sigma)_{yy}{}^2 + 4\tau_{xy}^2} + (\sigma_{xx}+\sigma_{yy})\sin\phi - 2c\cos\phi \tag{13}$$

Using the NS-FEM, the problem is discretized by N_e triangular elements and the total number of nodes is N_n. The smoothed strain rate $\tilde{\dot{\boldsymbol{\varepsilon}}}$ can be calculated from Eq. (1). The upper bound limit analysis for plane strain geomechanics problems using the Mohr–Coulomb failure criterion can be written as

$$\begin{aligned}\alpha^+ &= \min\left(\sum_{i=1}^{N_n} cA_i\cos\phi\sqrt{\left(\tilde{\dot{\varepsilon}}_{xx}^i-\tilde{\dot{\varepsilon}}_{yy}^i\right)^2+\left(\tilde{\dot{\gamma}}_{xy}^i\right)^2} - W_{\text{ext}}^0(\dot{\boldsymbol{u}})\right)\\ &= \min\left(\sum_{i=1}^{N_n} cA_i\beta_i\cos\phi - W_{\text{ext}}^0(\dot{\boldsymbol{u}})\right)\end{aligned} \tag{14a}$$

subject to

$$\left.\begin{aligned}&\dot{\boldsymbol{u}} = 0\ (\text{on } S_{\boldsymbol{u}})\\ &W_{\text{ext}}(\dot{\boldsymbol{u}}) = 1\\ &\tilde{\dot{\varepsilon}}_{xx}^i + \tilde{\dot{\varepsilon}}_{yy} = t_i\sin\phi\\ &t_i \geq \sqrt{\left(\tilde{\dot{\varepsilon}}_{xx}^i-\tilde{\dot{\varepsilon}}_{yy}^i\right)^2+\left(\tilde{\dot{\gamma}}_{xy}^i\right)^2}\ \ (i=1,2,\ldots,N_n)\end{aligned}\right\} \tag{14b}$$

where α^+ is the collapse load (i.e. in this study, α^+ is either the static or seismic bearing capacity factor), and A_i is the area of node i. The last constraint in Eq. (14b) is expressed in the conic form. As a result, the conic interior-point optimizer of the academic MOSEK package (MOSEK ApS, 2009) is used for solving this problem. The upper bound using the NS-FEM has been written using the Matlab language. The computations were performed on a Dell Optiplex 990 (Intel Core™ i5, 1.6 GHz CPU, 8 GB RAM) in a Windows XP environment.

3. Computation of static and seismic bearing capacity factors

Under seismic conditions, the three bearing capacity factors N_{cE}, N_{qE} and $N_{\gamma E}$ were solved independently. The seismic bearing capacity factors of strip footings were investigated separately for the effect of soil inertia forces (N_{cE}^s, N_{qE}^s and $N_{\gamma E}^s$) and superstructure inertia (N_{cE}^{ss}, N_{qE}^{ss} and $N_{\gamma E}^{ss}$) using the upper bound limit analysis based on NS-FEM. The numerical computation of the factors N_{cE}^s, N_{qE}^s and $N_{\gamma E}^s$ and N_{cE}^{ss}, N_{qE}^{ss} and $N_{\gamma E}^{ss}$ are compared with those results obtained using the method of characteristics reported by Cascone and Casablanca (2016) and others available in literature.

3.1. Effect of soil inertia on seismic bearing capacity factors

Based on the expression for the bearing capacity proposed by Terzaghi (1943), the ultimate load of strip footings under seismic conditions that only consider the inertia forces arising in the soil is conveniently expressed as follows:

$$q_{\text{ult}E}^s = cN_{cE}^s + qN_{qE}^s + \frac{1}{2}\gamma BN_{\gamma E}^s \tag{15}$$

where the seismic bearing capacity factors N_{cE}^s, N_{qE}^s and $N_{\gamma E}^s$ only account for the effect of soil inertia.

Fig. 2 illustrates the geometry and soil parameters to investigate the effect of soil inertia on the bearing capacity factors of strip footings. Due to the effects of an earthquake, the whole domain is considered, which should be large enough to eliminate the boundary effect on the solution, as shown in Fig. 2a–c. The typical finite element mesh and displacement conditions for the upper bound limit analysis of shallow strip foundations using NS-FEM are illustrated in Fig. 2d. The soil is described as a Mohr-Coulomb material with the cohesion c, unit weight γ and surcharge load q. The seismic acceleration coefficient is denoted as k_h and k_v in the horizontal and vertical directions, respectively, based on the pseudo-static approach. The horizontal displacements are free ($u \neq 0$) or fixed ($u = 0$) along the ground surface to describe the smooth or rough interface condition between the soil and the strip footings.

Without the soil weight, the seismic bearing capacity factor N_{cE}^s is analogous to the static factor N_c closed-form solution reported by Prandtl (1920). Later on, Reissner (1924) established the analytical

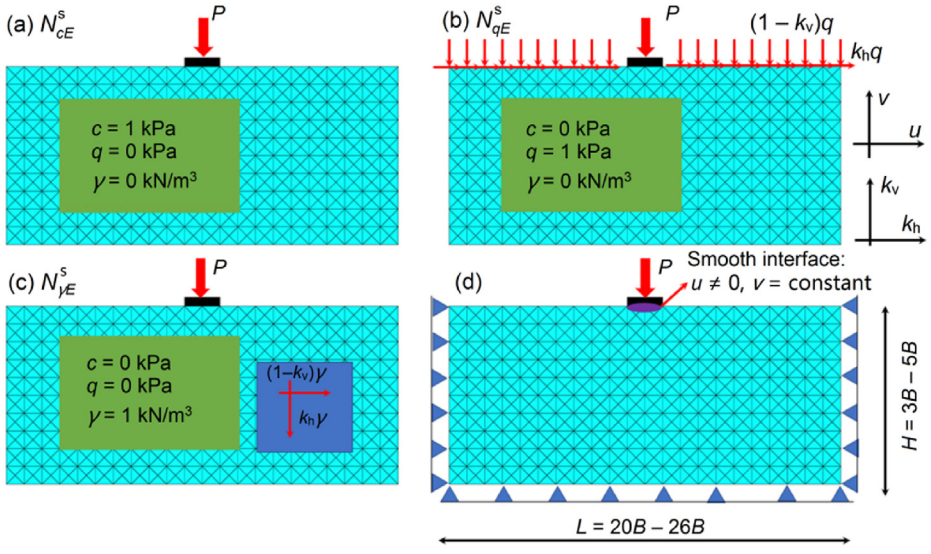

Fig. 2. The geometry and soil properties of the problem due to soil inertia.

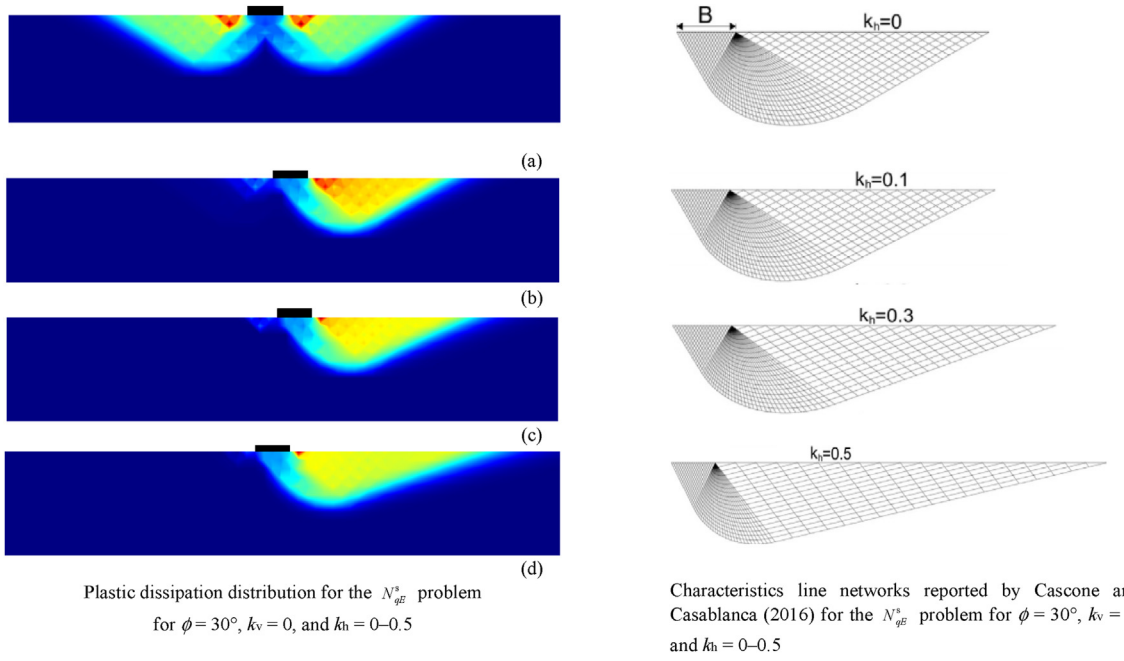

Plastic dissipation distribution for the N^s_{qE} problem for $\phi = 30°$, $k_v = 0$, and $k_h = 0–0.5$

Characteristics line networks reported by Cascone and Casablanca (2016) for the N^s_{qE} problem for $\phi = 30°$, $k_v = 0$, and $k_h = 0–0.5$

Fig. 3. Comparisons of plastic dissipation distribution with the characteristics line networks for the N^s_{qE} problem for $\phi = 30°$, and $k_v = 0$: (a) $k_h = 0$, (b) $k_h = 0.1$, (c) $k_h = 0.3$, and (d) $k_h = 0.5$.

formulation for the static bearing capacity N_q based on the Prandtl failure mechanism.

In order to calculate the seismic term N^s_{qE}, the typical mesh illustrated in Fig. 2b and the soil parameters $c = 0$ kPa, $q = 1$ kPa, and $\gamma = 0$ kN/m^3 are considered. The upper bound limit analysis for plane strain problems using NS-FEM can be determined by minimizing the collapse load $N^s_{qE} = \alpha^+ = \min\left(-W^0_{\text{ext}}(\dot{\boldsymbol{u}})\right)$.

Fig. 3 shows a comparison of plastic dissipation distribution using NS-FEM with that obtained by the characteristics line networks reported by Cascone and Casablanca (2016) in the case of $\phi = 30°$, $k_v = 0$, and $k_h = 0–0.5$. The power dissipations based on the NS-FEM are almost identical with those using the slip-line method from Cascone and Casablanca (2016). Under static conditions, the failure mechanism is symmetrical. Under seismic conditions, the failure pattern becomes asymmetrical. For increasing k_h, the larger inertia force in the soil mass must be balanced, and the failure zone becomes longer.

To show the efficiency of the seismic bearing capacity factors using NS-FEM, we consider the computational cost based on the number of variables and CPU times for the terms N^s_{qE} and $N^s_{\gamma E}$ (smooth interface) in the case of $\phi = 30°$, $k_h = 0.3$, and $k_v = 0$. The reported CPU times refer to the time spent on the interior-point iterations for solving the seismic bearing capacity factors. The factors N^s_{qE} and $N^s_{\gamma E}$, the number of variables N_{var} and the CPU time obtained by the finite element analysis using triangular elements (FEM-T3), the edge-based smoothed FEM (ES-FEM-T3), and the NS-FEM using triangular elements (NS-FEM-T3) are summarized in Tables 1 and 2.

The convergence rate archived by the present method (NS-FEM) is compared with those obtained by FEM-T3 and ES-FEM-T3, as shown in Fig. 4. Although the coarse mesh is used, the seismic bearing capacity factors N^s_{qE} and $N^s_{\gamma E}$ using the NS-FEM are more convergent than other existing methods such as FEM and ES-FEM using triangle elements. In addition, with the same number of elements, the total number of NS-FEM variables is smaller than those of FEM-T3 and ES-FEM-T3. Regarding the maximum number of variables ($N_{\text{var}} = 40{,}046$), according to the CPU time for solving the optimization problem using NS-FEM based on the interior-point algorithm, very fast convergence is attained using the NS-FEM limit analysis (i.e. the CPU time of 5.8 s). These comparisons prove the effectiveness and rapid convergence of the NS-FEM when using the MOSEK optimizer to solve large sparse SOCP problems.

We conducted several simulations for the case of $\phi = 0°$, in which the Mohr–Coulomb condition reduces to the unbonded Tresca yield criterion for plane strain problems, as noted in Tin-Loi and Ngo (2003), Vicente da Silva and Antao (2007) and Ciria et al. (2008). The numerical results are given in Table 3 for the cases of $k_h = 0–0.5$

Table 1
Comparisons of seismic bearing capacity factor N^s_{qE} using the NS-FEM and other solutions ($\phi = 30°$, k_h= 0.3 and k_v= 0, smooth interface).

N_e	FEM-T3			ES-FEM-T3			Presnet method (NS-FEM)		
	N_{var}	CPU time (s)	N^s_q	N_{var}	CPU time (s)	N^s_q	N_{var}	CPU time (s)	N^s_q
320	1331	0.39	29.3442	1883	0.36	25.764	926	0.34	18.1526
1280	5219	0.47	21.7552	7283	0.92	20.1364	3446	0.59	16.1102
2880	11,667	1.25	19.4753	16203	3.39	18.4169	7566	1.01	15.6655
5120	20,675	1.95	18.325	28,643	4.75	17.5217	13,286	1.77	15.4055
8000	32,243	3.05	17.6708	44,603	11.25	16.9861	20,606	2.86	15.3485
11,520	46,371	5.06	17.1648	64,083	19.73	16.618	29,526	4.08	15.0919

Note: $N_{\text{var}} = 2N_n + 3N_e$ for FEM-T3, $N_{\text{var}} = 2N_n + 3N_{ed}$ for ES-FEM-T3, $N_{\text{var}} = 5N_n$ for NS-FEM, where N_{var}, N_n, N_e, and N_{ed} are the numbers of variables, nodes, triangular elements, and triangular edges in the problems, respectively.

Table 2
Comparisons of seismic bearing capacity factor $N^s_{\gamma E}$ using the NS-FEM and other solutions ($\phi = 30°$, $k_h = 0.3$, $k_v = 0$, smooth interface).

N_e	FEM-T3			ES-FEM-T3			Presnet method (NS-FEM)		
	N_{var}	CPU time (s)	N^s_γ	N_{var}	CPU time (s)	N^s_γ	N_{var}	CPU time (s)	N^s_γ
320	1331	0.38	19.2639	1883	0.47	17.4831	926	0.39	8.2468
720	2955	0.45	14.7098	4143	0.75	13.6932	1986	0.45	7.7182
1280	5219	0.52	12.7074	7283	1.19	11.9484	3446	0.58	7.1805
2000	8123	0.77	11.4794	11,303	2.25	10.8873	5306	0.7	7.0786
2880	11,667	1.55	10.5981	16,203	3.8	10.1541	7566	0.98	6.9613
3920	15,851	1.69	10.0242	21,983	6.09	9.6542	10,226	1.31	6.8742
5120	20,675	2.39	9.6112	28,643	6.28	9.2856	13,286	1.63	6.86
6480	26,139	2.94	9.2687	36,183	9.75	8.9866	16,746	2.2	6.8344
8000	32,243	3.63	9.0161	44,603	12.63	8.7729	20,606	2.83	6.8281
9680	38,987	4.36	8.8101	53,903	17.39	8.5738	24,866	3.38	6.8277
11,520	46,371	5.58	8.6327	64,083	24.16	8.4192	29,526	3.7	6.8188
15,680	63,059	9.06	8.3678	87,083	30.27	8.1231	40,046	5.8	6.8028

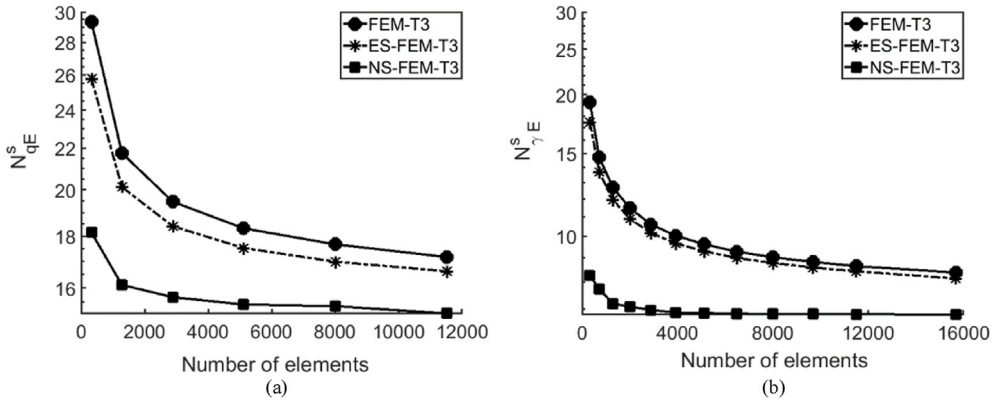

Fig. 4. The convergence rate of seismic bearing capacity factors in the case of $\phi = 30°$, $k_h = 0.3$ and $k_v = 0$: (a) N^s_{qE}, and (b) $N^s_{\gamma E}$ (smooth interface).

Table 3
The seismic bearing capacity factor N_{cE} for the case of $\phi = 0°$, $k_h = 0–0.5$, and $k_v = 0$.

Number of element	N_{cE}					
	$k_h = 0$	$k_h = 0.1$	$k_h = 0.2$	$k_h = 0.3$	$k_h = 0.4$	$k_h = 0.5$
160	5.93	5.92	5.47	4.83	4.26	3.75
640	5.43	5.25	4.63	3.96	3.36	2.88
1440	5.33	5.1	4.44	3.68	3.05	2.58
2560	5.28	5.02	4.37	3.55	2.9	2.43
4000	5.25	4.97	4.33	3.48	2.81	2.34
5760	5.24	4.94	4.3	3.44	2.75	2.28
7840	5.22	4.92	4.28	3.41	2.71	2.24
10,240	5.21	4.9	4.26	3.39	2.68	2.2
12,960	5.2	4.88	4.25	3.37	2.65	2.18
16,000	5.2	4.87	4.24	3.36	2.64	2.16

and $k_v = 0$. In this case, the stable convergence of solutions and the accurate values of collapse loads as shown in Fig. 5 prove that the numerical approach is naturally "immune" from the volumetric locking. Readers are referred to Meng et al. (2020) who stated that the application of NS-FEM and SOCP to elastoplastic analysis of static problems is free from the volumetric locking while using the low-order mixed element. In that study, the well-known "overly stiff" phenomenon was addressed by varying the Poisson's ratio from 0.4 to 0.49999, while the solution still becomes stable and accurate. In addition, the special arrangement of linear elements (Fig. 2), in which four elements form a rectangle domain with the central node in the intersection of the diagonals, can eliminate the locking phenomenon as noted in Vicente da Silva and Antao (2007). Readers can refer to Sloan and Kleeman (1995) who reported that the volume locking can be removed by increasing the ratio between the number of compatibility conditions and the number of degrees of freedom used in the discretization in the optimization problem.

The seismic bearing capacity factor N^s_{qE} calculated when the friction angle ϕ ranges from 15° to 45°, and the value of k_h varies from 0 to 0.8 is listed in Table 4. The obtained results agree well with those from the characteristics method given by Cascone and Casablanca (2016), and the errors are within 5%. The variation of N^s_{qE} with the horizontal earthquake acceleration coefficient k_h is shown in Fig. 6a. The computational results indicate that for given values of φ, the bearing capacity factor N^s_{qE} decreases continuously with an increasing k_h. Fig. 6b shows the effect of vertical seismic acceleration coefficient k_v on the bearing capacity factor N^s_{qE}. An upward vertical seismic acceleration ($k_v > 0$) leads to a reduction in the magnitude of N^s_{qE}. In contrast, the seismic term N^s_{qE} increases with vertical seismic acceleration in the downward direction, which means that a negative value of k_v leads to an increase in the vertical component of the surcharge.

Unlike N^s_{cE} andN^s_{qE}, the bearing capacity factor $N^s_{\gamma E}$ mainly depends on the roughness of the soil–foundation interaction interface. To calculate the seismic term $N^s_{\gamma E}$, the typical mesh illustrated in Fig. 2c and the soil parameters $c = 0$ kPa, $q = 0$ kPa, and $\gamma = 1$ kN/m^3 are considered. The plane strain optimization problem using NS-FEM can be determined as $N^s_{\gamma E} = \alpha^+ = \min\left(-W^0_{ext}(\dot{\boldsymbol{u}})\right)$. The lateral displacement of nodes in contact with the footing is free or fixed to describe smooth or rough interface conditions between the footing and the soil, respectively.

The computed values of bearing capacity factor $N^s_{\gamma E}$ of strip footing for $\phi = 15°–45°$, $k_h = 0–0.8$ and $k_v = 0$ using NS-FEM are

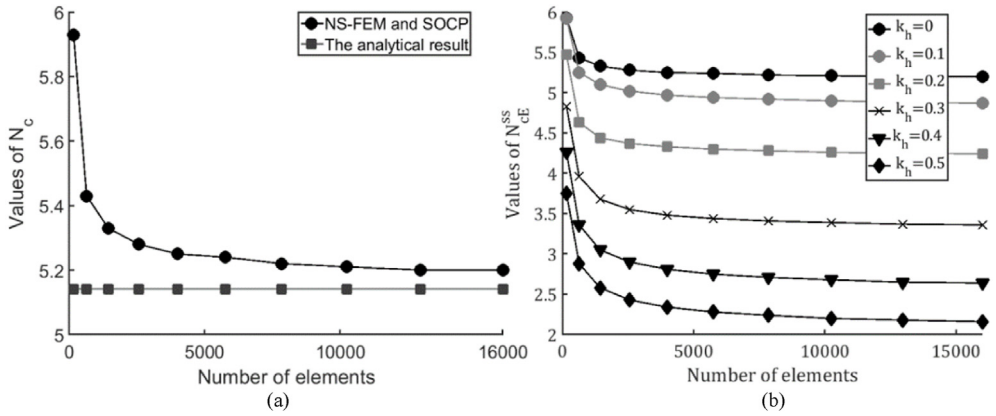

Fig. 5. Calculation of (a) static and (b) seismic bearing capacity factors for $\phi = 0°$, $k_h = 0–0.5$ and $k_v = 0$.

Table 4
Seismic bearing capacity factor N^s_{qE} of strip footing ($k_v = 0$).

k_h	N^s_{qE}						
	$\phi = 15°$	$\phi = 20°$	$\phi = 25°$	$\phi = 30°$	$\phi = 35°$	$\phi = 40°$	$\phi = 45°$
0	4.02	6.52	10.82	18.63	33.43	63.76	134.95
0.05	3.87	6.34	10.57	18.21	32.91	62.94	132.75
0.1	3.71	6.07	10.18	17.71	32.07	61.7	129.22
0.15	3.49	5.82	9.85	17.15	31.33	60.34	126.58
0.2	3.19	5.48	9.41	16.53	30.26	58.89	125.14
0.25	2.74	5.07	8.92	15.84	29.37	57.23	121.42
0.3	–	4.58	8.36	15.09	28.15	55.6	117.91
0.35	–	3.83	7.7	14.27	27.1	53.69	115.14
0.4	–	–	6.94	13.48	25.85	51.93	110.4
0.45	–	–	5.86	12.34	24.48	49.74	107.54
0.5	–	–	–	11.16	22.98	47.9	103.68
0.55	–	–	–	9.63	21.38	45.14	101.43
0.6	–	–	–	–	19.41	43.48	98.17
0.65	–	–	–	–	17.4	40.24	94.77
0.7	–	–	–	–	14.75	37.84	91.21
0.75	–	–	–	–	–	34.97	87.49
0.8	–	–	–	–	–	31.5	83.58

summarized in Table 5 (for smooth and rough footings) and plotted in Fig. 7. Under static condition ($k_h = 0$), the values of bearing capacity factor $N^s_{\gamma E}$ of strip footing are in good agreement with those from the following theories: (i) Cascone and Casablanca (2016) using the method of characteristics; (ii) Martin (2005) calculating the exact vertical bearing capacity of strip footing on Mohr–Coulomb soil using the method of characteristics by ABC computer program; and (iii) Hjiaj et al. (2005) using the lower and upper bound limit analysis in combination with the FEM and nonlinear programming. According to Meyerhof (1963), the static values of N_γ for the rough interface are almost twice those for the smooth interface. Under seismic conditions, the bearing capacity factor $N^s_{\gamma E}$ of strip footing for smooth and rough footings agree well with those reported by Cascone and Casablanca (2016), and the errors are within 5%.

Fig. 7c and d shows the variation in $N^s_{\gamma E}$ with various k_v/k_h ratios for the case of $\phi = 30°$. The seismic bearing capacity factor $N^s_{\gamma E}$ reduces with an increasing upward vertical acceleration (positive values of k_v/k_h). In contrast, the factor $N^s_{\gamma E}$ increases continuously with the vertical seismic acceleration in the downward direction ($k_v/k_h = -1$).

To consider the effect of soil inertia on the bearing capacity factors of strip footings, the corrective coefficients $e^s_{qE} = N^s_{qE}/N_q$ and $e^s_{\gamma E} = N^s_{\gamma E}/N_\gamma$ are defined as the ratios of the factors N^s_{qE} and $N^s_{\gamma E}$ under seismic condition to the factors N_q and N_γ under static condition, respectively. Fig. 8a–c presents the variations of corrective coefficients with the change of the k_v/k_h ratio in the case of $\phi = 30°$. The corrective coefficients e^s_{qE} and $e^s_{\gamma E}$ reduce with an increasing upward vertical acceleration (positive values of k_v/k_h). In contrast, the factors e^s_{qE} and $e^s_{\gamma E}$ increase continuously with vertical seismic acceleration in the downward direction ($k_v/k_h = -1$).

3.2. Effect of superstructure inertia on seismic bearing capacity factors

The ultimate load of strip footings under seismic conditions that only consider superstructure inertia is expressed as the following formulation:

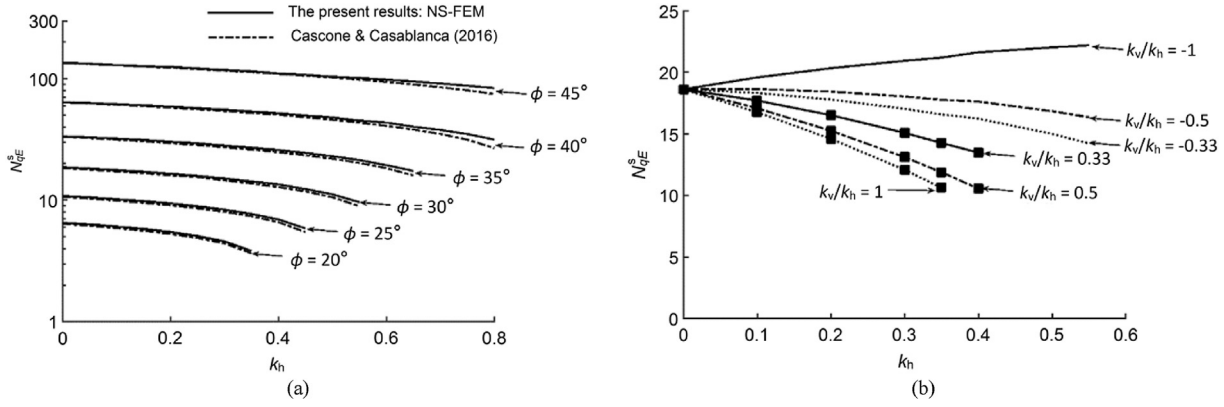

Fig. 6. Seismic bearing capacity factor N^s_{qE}: (a) Effect of horizontal acceleration; and (b) Effect of vertical acceleration for the case of $\phi = 30°$.

Table 5
Seismic bearing capacity factor $N^s_{\gamma E}$ of strip footing ($k_v = 0$).

k_h	$N^s_{\gamma E}$ (smooth interface)							$N^s_{\gamma E}$ (rough interface)						
	$\phi = 15°$	$\phi = 20°$	$\phi = 25°$	$\phi = 30°$	$\phi = 35°$	$\phi = 40°$	$\phi = 45°$	$\phi = 15°$	$\phi = 20°$	$\phi = 25°$	$\phi = 30°$	$\phi = 35°$	$\phi = 40°$	$\phi = 45°$
0	0.79	1.65	3.54	7.68	17.84	43.65	117.73	1.27	2.91	6.53	14.97	35.37	86.1	238.77
0.05	0.74	1.63	3.52	7.66	17.25	41.42	114.67	1.22	2.84	6.2	14.23	34.67	83.45	230.57
0.1	0.7	1.59	3.47	7.59	17.14	40.77	112.21	1.12	2.66	5.97	13.45	32.04	81.2	223.19
0.15	0.63	1.51	3.38	7.47	16.96	39.52	109.76	0.98	2.5	5.65	12.85	30.91	78.57	216.18
0.2	0.5	1.39	3.25	7.31	16.69	38.98	106.62	0.79	2.25	5.31	12.31	29.45	74.89	210.69
0.25	0.32	1.24	3.08	7.08	16.41	38.38	104.46	0.45	1.98	4.93	11.67	28.03	71.91	203.87
0.3	–	1.02	2.85	6.8	16.15	37.7	99.75	–	1.64	4.48	10.98	26.83	69.06	197.45
0.35	–	0.67	2.55	6.45	15.59	36.95	94.48	–	1.12	3.96	10.21	25.51	66.53	190.34
0.4	–	–	2.21	6.05	15.07	36.12	91.17	–	–	3.33	9.34	24.08	63.84	183.89
0.45	–	–	1.54	5.47	14.37	35.19	88.32	–	–	2.48	8.32	22.52	60.94	176.45
0.5	–	–	–	4.76	13.45	34.16	83.27	–	–	–	7.18	20.8	57.84	169.12
0.55	–	–	–	3.78	12.48	32.99	79.33	–	–	–	5.64	18.86	54.48	160.78
0.6	–	–	–	–	11.24	31.62	76.65	–	–	–	–	16.61	50.85	152.89
0.65	–	–	–	–	9.55	29.91	73.76	–	–	–	–	13.85	46.86	144.56
0.7	–	–	–	–	6.38	26.73	70.65	–	–	–	–	9.71	42.42	135.43
0.75	–	–	–	–	–	24.09	67.24	–	–	–	–	–	37.34	126.73
0.8	–	–	–	–	–	20.69	63.38	–	–	–	–	–	31.32	116.78

$$q^{ss}_{ultE} = cN^{ss}_{cE} + qN^{ss}_{qE} + \frac{1}{2}\gamma BN^{ss}_{\gamma E} \quad (16)$$

where the three terms N^{ss}_{cE}, N^{ss}_{qE} and $N^{ss}_{\gamma E}$ only account for the effect of superstructure inertia on the seismic bearing capacity.

Fig. 9 illustrates the geometry and soil parameters to investigate the effect of superstructure inertia on the bearing capacity factors of strip footings. Due to the effects of seismic force, the rectangular domain is considered large enough to eliminate the boundary effect on the solution, as shown in Fig. 9a–c. The typical finite element mesh and displacement conditions for the upper bound limit analysis of shallow strip foundations using NS-FEM are illustrated in Fig. 9d.

Figs. 10–12 show the power dissipation and displacement fields for strip footing problems using NS-FEM compared with the characteristics line networks reported by Cascone and Casablanca (2016) for $\phi = 30°$, $k_v = 0$, and $k_h = 0–0.5$. Under static conditions ($k_h = 0$), the failure mechanism of shallow strip foundations is symmetrical, as shown in Figs. 10a, 11a and 12a. Under seismic conditions ($k_h > 0$), the failure mechanisms become asymmetrical and identical to that of the characteristic line networks using the slip-line method from Cascone and Casablanca (2016). With an

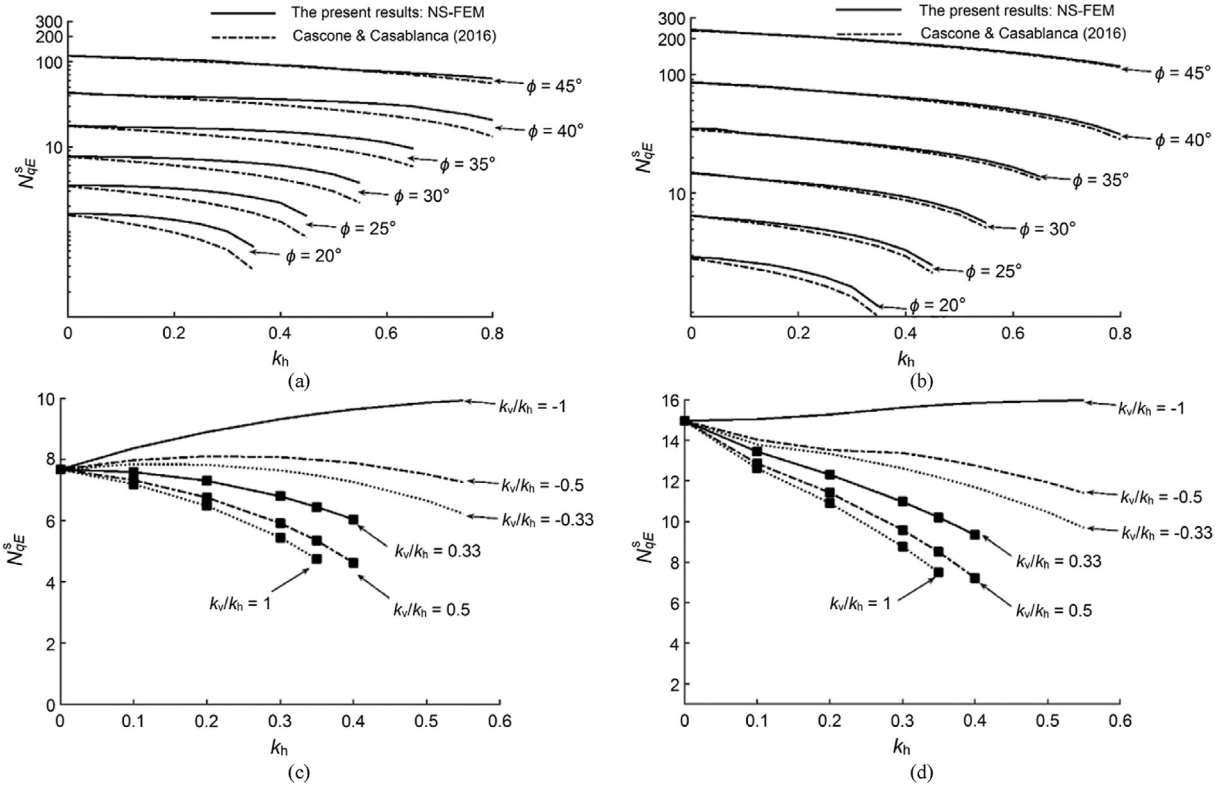

Fig. 7. Seismic bearing capacity factor $N^s_{\gamma E}$: (a) Effect of horizontal acceleration for the smooth foundation; (b) Effect of horizontal acceleration for the rough foundation; (c) Effect of vertical acceleration for the smooth foundation ($\phi = 30°$); and (d) Effect of vertical acceleration for the rough foundation ($\phi = 30°$).

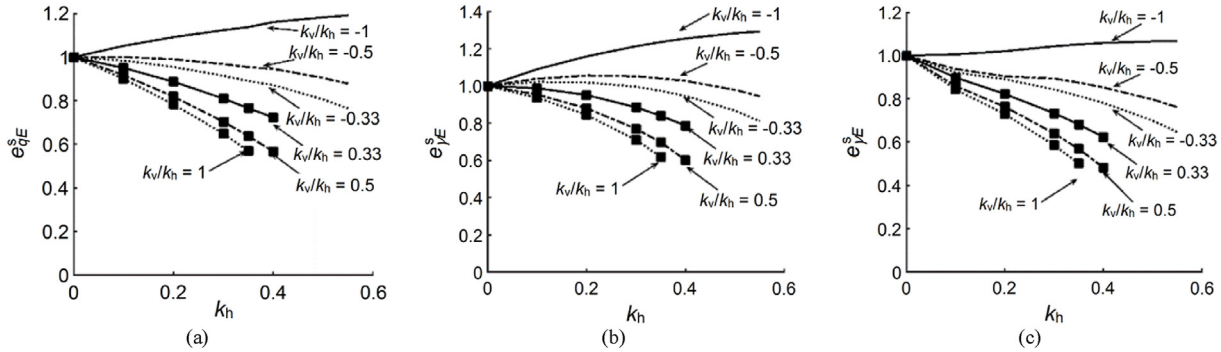

Fig. 8. Effect of k_v on the corrective coefficients for the case of $\phi = 30°$: (a) e^s_{qE}, and (b) $e^s_{\gamma E}$ for smooth foundation; and (c) $e^s_{\gamma E}$ for rough foundation.

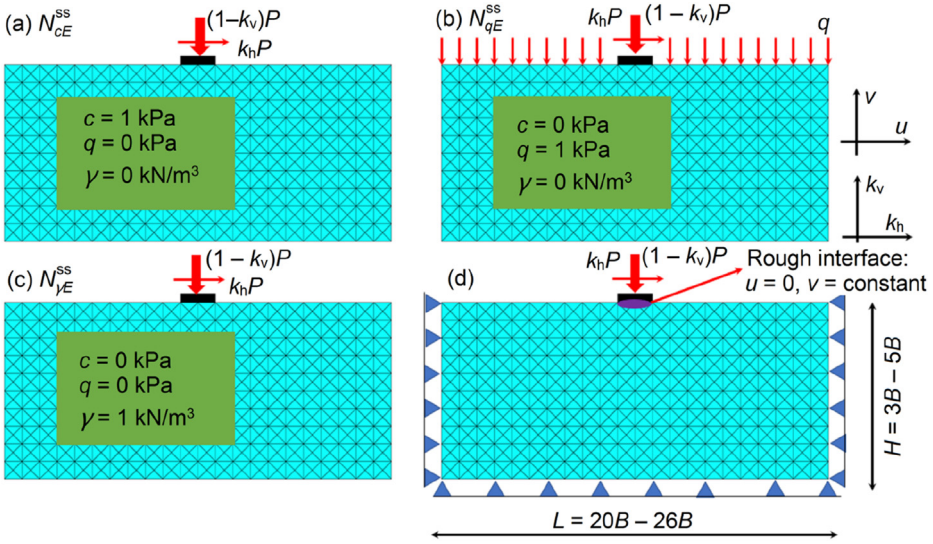

Fig. 9. The geometry and soil properties of the problem due to superstructure inertia.

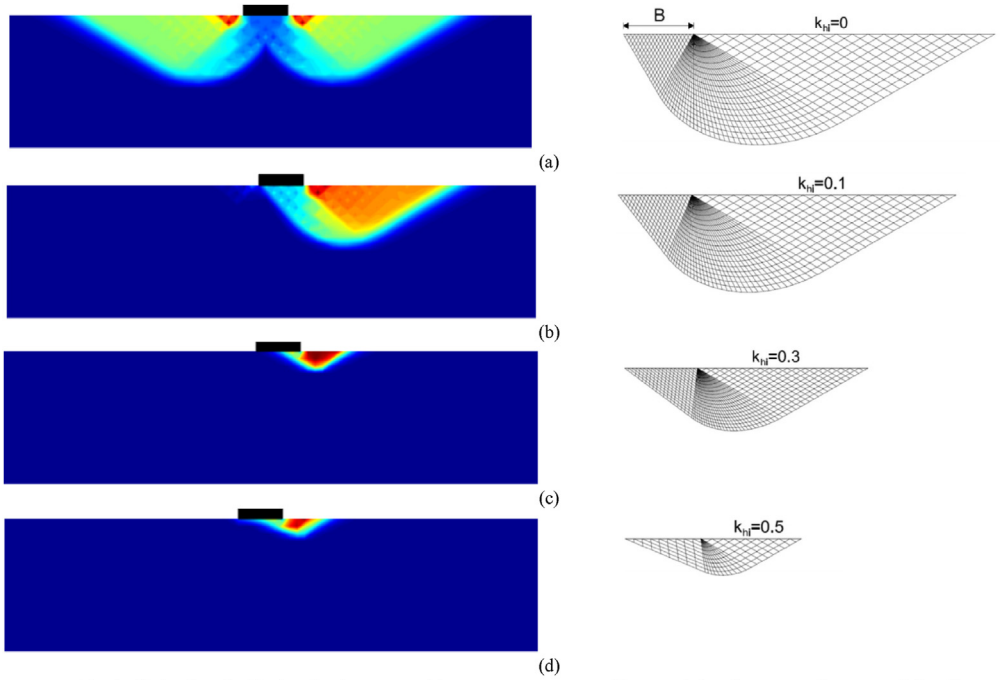

Plastic dissipation distribution for the N^{ss}_{cE} problem for $\phi = 30°$, $k_v = 0$, and $k_h = 0–0.5$

Characteristics line networks reported by Cascone and Casablanca (2016) for the N^{ss}_{cE} problem for $\phi = 30°$, $k_v = 0$, and $k_h = 0–0.5$

Fig. 10. Comparisons of plastic dissipation distribution with the characteristics line networks for the N^{ss}_{cE} problem for $\phi = 30°$, $k_v = 0$: (a) $k_h = 0$, (b) $k_h = 0.1$, (c) $k_h = 0.3$, and (d) $k_h = 0.5$.

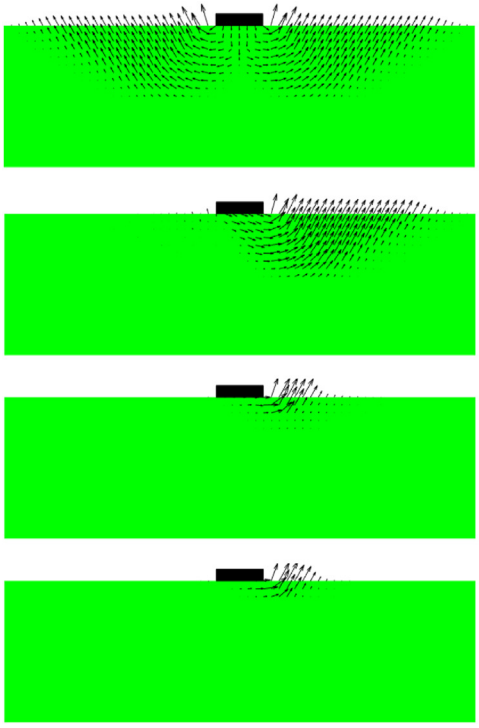

Displacement field for the $N_{\gamma E}^{ss}$ problem with smooth interface for $\phi = 30°$, $k_v = 0$, and $k_h = 0$–0.5

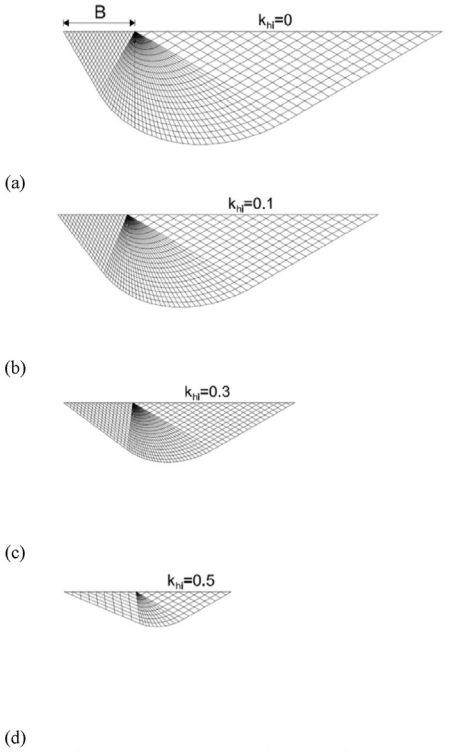

Characteristics line networks reported by Cascone and Casablanca (2016) for the $N_{\gamma E}^{ss}$ problem for $\phi = 30°$, $k_v = 0$, and $k_h = 0$–0.5 (the Hill's failure mechanism)

Fig. 11. Comparisons of displacement fields with the Hill's failure mechanism for the $N_{\gamma E}^{ss}$ problem with smooth interface for $\phi = 30°$ and $k_v = 0$: (a) $k_h = 0$, (b) $k_h = 0.1$, (c) $k_h = 0.3$, and (d) $k_h = 0.5$.

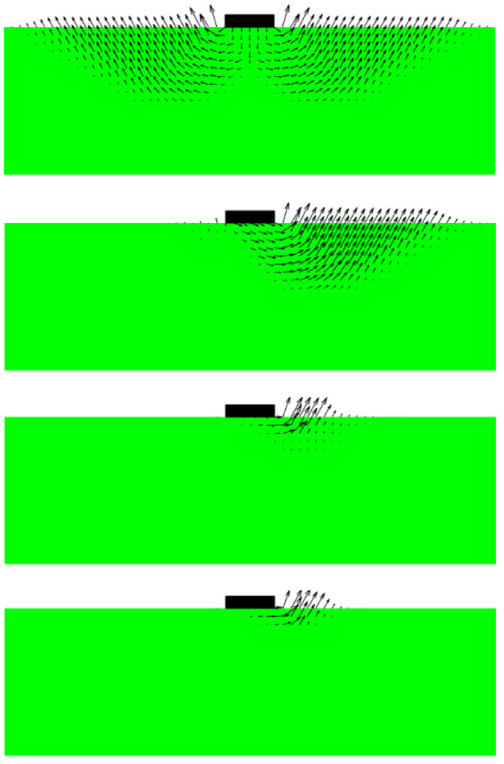

Displacement field for the $N_{\gamma E}^{ss}$ problem with rough interface for $\phi = 30°$, $k_v = 0$, and $k_h = 0$–0.5

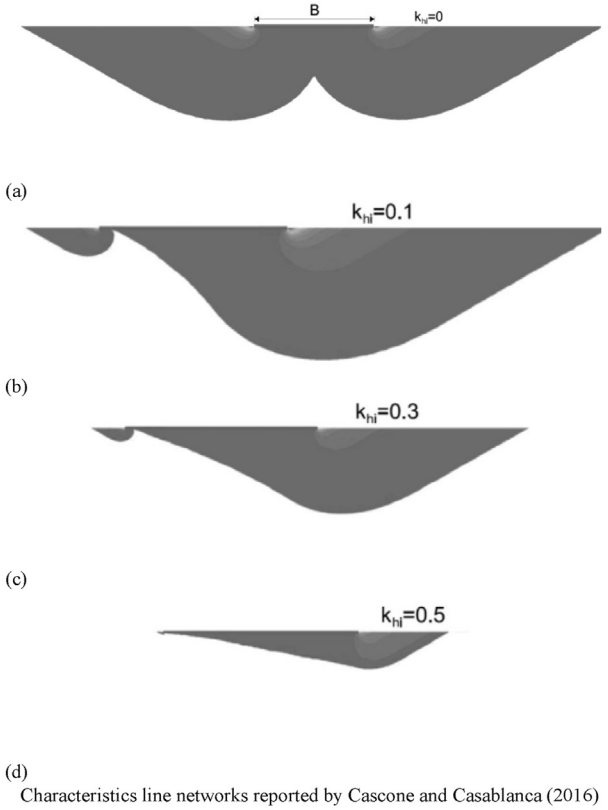

Characteristics line networks reported by Cascone and Casablanca (2016) for the $N_{\gamma E}^{ss}$ problem for $\phi = 30°$, $k_v = 0$, and $k_h = 0$–0.5 (the Prandtl's failure mechanism)

Fig. 12. Comparisons of displacement fields with the Prandtl's failure mechanism for the $N_{\gamma E}^{ss}$ problem with smooth interface for $\phi = 30°$ and $k_v = 0$: (a) $k_h = 0$, (b) $k_h = 0.1$, (c) $k_h = 0.3$, and (d) $k_h = 0.5$.

Table 6
Seismic bearing capacity factors N_{cE}^{ss} and N_{qE}^{ss} of strip footing ($k_v = 0$).

k_h	N_{cE}^{ss}							N_{qE}^{ss}						
	$\phi = 15°$	$\phi = 20°$	$\phi = 25°$	$\phi = 30°$	$\phi = 35°$	$\phi = 40°$	$\phi = 45°$	$\phi = 15°$	$\phi = 20°$	$\phi = 25°$	$\phi = 30°$	$\phi = 35°$	$\phi = 40°$	$\phi = 45°$
0	11.23	15.16	21.05	30.44	46.87	75.03	134.03	4.02	6.52	10.82	18.63	33.43	63.76	134.95
0.05	10.97	14.62	20.04	28.27	43.62	70.12	121.8	3.77	6.08	10.04	17.23	30.75	58.41	120.59
0.1	9.98	13.22	18.07	25.69	38.43	61.11	107.08	3.48	5.6	9.19	15.63	27.68	52.09	105.91
0.15	9.73	12.72	17.28	23.24	36.09	56.43	95.11	3.14	5.08	8.33	14.1	24.68	45.81	92.08
0.2	8.39	11.01	14.9	20.88	30.58	47.35	79.31	2.74	4.53	7.46	12.59	21.93	40.23	79.94
0.25	7.89	10.4	13.97	18.6	28.18	42.89	68.92	2.27	3.94	6.58	11.12	19.28	35.14	69.28
0.3	–	8.86	11.88	16.47	23.75	36.01	57.36	–	3.34	5.69	9.68	16.78	30.28	59.62
0.35	–	7.88	10.52	14.46	20.65	32.35	51.45	–	2.86	4.91	8.36	14.46	25.97	51.51
0.4	–	–	9.23	12.67	18.07	27.78	43.02	–	–	4.27	7.31	12.65	22.72	45.17
0.45	–	–	7.99	11.26	15.36	23.86	38.53	–	–	3.65	6.45	11.18	20.12	37.9
0.5	–	–	–	10.34	14.35	21.3	33.66	–	–	–	5.62	9.81	17.77	33.41
0.55	–	–	–	9.09	12.51	18.08	29.42	–	–	–	4.79	8.55	15.62	29.45
0.6	–	–	–	–	10.81	16.6	25.73	–	–	–	–	7.40	13.66	25.95
0.65	–	–	–	–	9.32	13.56	21.97	–	–	–	–	6.31	11.89	21.74
0.7	–	–	–	–	7.98	12.96	19.75	–	–	–	–	5.27	9.98	18.85
0.75	–	–	–	–	–	11.4	15.96	–	–	–	–	–	8.56	16.35
0.8	–	–	–	–	–	9.81	13.48	–	–	–	–	–	7.23	14.14

Table 7
Seismic bearing capacity factor $N_{\gamma E}^{ss}$ of strip footing ($k_v = 0$).

k_h	$N_{\gamma E}^{ss}$ (smooth interface)							$N_{\gamma E}^{ss}$ (rough interface)						
	$\phi = 15°$	$\phi = 20°$	$\phi = 25°$	$\phi = 30°$	$\phi = 35°$	$\phi = 40°$	$\phi = 45°$	$\phi = 15°$	$\phi = 20°$	$\phi = 25°$	$\phi = 30°$	$\phi = 35°$	$\phi = 40°$	$\phi = 45°$
0.00	0.79	1.65	3.54	7.68	17.84	43.65	117.73	1.29	3.11	6.92	15.57	36.37	87.1	240.77
0.05	0.61	1.49	2.99	6.53	14.92	37.22	98.75	1.18	2.82	5.98	13.51	32.17	76.7	204.19
0.1	0.48	1.18	2.43	5.58	12.64	29.48	78.93	1.03	2.4	5.35	11.81	26.69	66.71	172.47
0.15	0.39	0.97	2.09	4.33	10.02	24.57	66.7	0.87	2.06	4.68	10.37	23.43	54.91	149.76
0.2	0.29	0.67	1.62	3.47	7.91	19.68	49.64	0.69	1.79	3.86	8.97	18.7	45.7	119.32
0.25	0.18	0.56	1.26	3.12	6.96	16.09	38.7	0.49	1.38	3.03	6.91	15.7	37.05	94.46
0.3	–	0.34	0.93	2.65	4.85	12.59	30.69	–	1.06	2.41	5.4	12.55	28.81	74.58
0.35	–	0.24	0.73	1.86	3.93	9.04	24.39	–	0.75	1.86	4.29	10.13	25.59	57.02
0.4	–	–	0.49	1.5	3.03	7.1	18.97	–	–	1.38	3.57	8.05	18.48	44.84
0.45	–	–	0.31	1.12	2.37	5.38	14.43	–	–	0.89	2.74	6.29	15.89	36.11
0.5	–	–	–	0.78	1.67	3.98	11.65	–	–	–	2.02	4.82	11.29	27.35
0.55	–	–	–	0.42	1.32	2.98	7.93	–	–	–	1.42	3.18	8.09	21.03
0.6	–	–	–	–	0.89	2.39	5.95	–	–	–	–	2.42	6.1	16.55
0.65	–	–	–	–	0.63	1.69	4.86	–	–	–	–	1.67	4.56	12.52
0.7	–	–	–	–	0.29	1.34	3.87	–	–	–	–	–	2.92	9.13
0.75	–	–	–	–	–	0.89	2.67	–	–	–	–	–	2.02	6.92
0.8	–	–	–	–	–	0.56	1.84	–	–	–	–	–	1.42	5.08

increasing value of k_h, the seismic beaering capacity factors reduces significantly due to inclination of the applied load acting on the shallow foundation, leading to the observation that the length and the depth of failure zones become shallower than those for the case of $k_h = 0$, as shown in Fig. 10b–d, 11b–d, and 12b–d.

The seismic bearing capacity factors due to superstructure inertia effect calculated for $\phi = 15°–45°$ and $k_h = 0–0.8$ are listed in Table 6 for N_{cE}^{ss} and N_{qE}^{ss} and Table 7 for $N_{\gamma E}^{ss}$, corresponding to the Hill's and Prandtl's failure mechanisms, respectively, as noted by Casablanca et al. (2021). The terms N_{cE}^{ss}, N_{qE}^{ss} and $N_{\gamma E}^{ss}$ using NS-FEM are plotted with changes in k_h and ϕ, as shown in Fig. 13. The computational results indicate that for given values of friction angle ϕ, the bearing capacity factors decrease continuously with an increase in the horizontal earthquake acceleration coefficient k_h. Although the obtained results of N_{cE}^{ss}, N_{qE}^{ss} and $N_{\gamma E}^{ss}$ using the NS-FEM are slightly higher than those reported by Cascone and Casablanca (2016), the errors are within 5%. Therefore, the numerical results given in Tables 6 and 7 illustrate the capability and effectiveness of the NS-FEM approach for computing upper bounds of seismic bearing capacity factors of strip footings.

To consider the effect of superstructure inertia on the bearing capacity of strip footings, corrective coefficients $e_{iE}^{ss} = N_{iE}^{ss}/N_i$ ($i = c$, q, γ) are defined as the ratio of the factor N_{iE}^{ss} under seismic conditions to N_i under static conditions. Fig. 14 shows the variation of the corrective coefficients e_{iE}^{ss} with the horizontal earthquake acceleration coefficient k_h in the case of $k_v = 0$. Values of e_{iE}^{ss} agree well with those given by Cascone and Casablanca (2016). Under superstructure inertia effect, Fig. 14a and b illustrates that the reductions of corrective coefficients e_{cE}^{ss} and e_{qE}^{ss} depend on k_h and ϕ. On the other hand, $e_{\gamma E}^{ss}$ decreases with an increase in k_h and less depends on ϕ, and the reduction rate tends to increase rapidly for the higher acceleration of earthquake, as shown in Fig. 14c and d.

The effect of the vertical acceleration k_v on the bearing capacity factors based on the ratio k_v/k_h is summarized in Table 8 for the case of $\phi = 30°$. The seismic terms N_{cE}^{ss}, N_{qE}^{ss} and $N_{\gamma E}^{ss}$ decrease with changes in k_v/k_h. It means that the reduction of load transmitted from the structure to the foundation significantly impacts the seismic terms N_{cE}^{ss}, N_{qE}^{ss} and $N_{\gamma E}^{ss}$.

3.3. The link between the static and seismic bearing capacity factors

For practical application, the seismic bearing capacity of strip footings can be evaluated by the combination of the effect of soil and superstructure inertia as follows:

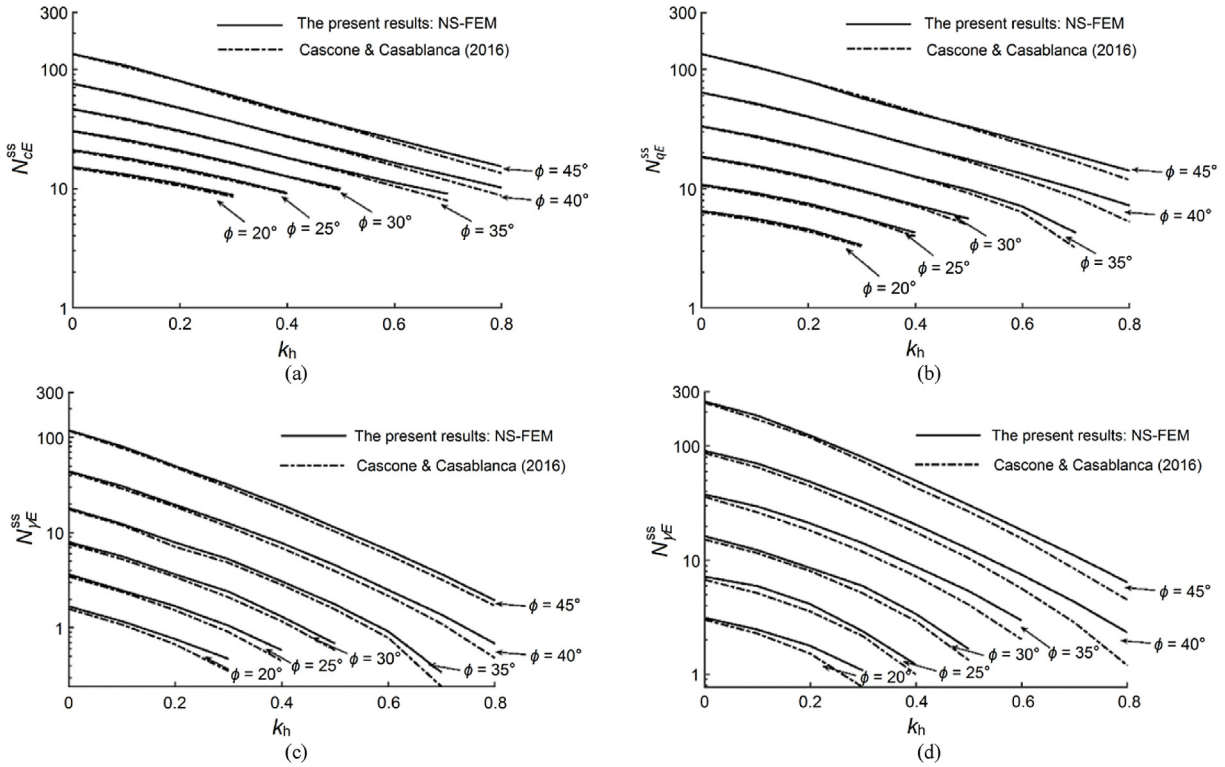

Fig. 13. Effect of superstructure horizontal acceleration k_h on seismic bearing capacity factors: (a) N_{cE}^{ss}, (b) N_{qE}^{ss}, (c) $N_{\gamma E}^{ss}$ for smooth foundation, and (d) $N_{\gamma E}^{ss}$ for rough foundation.

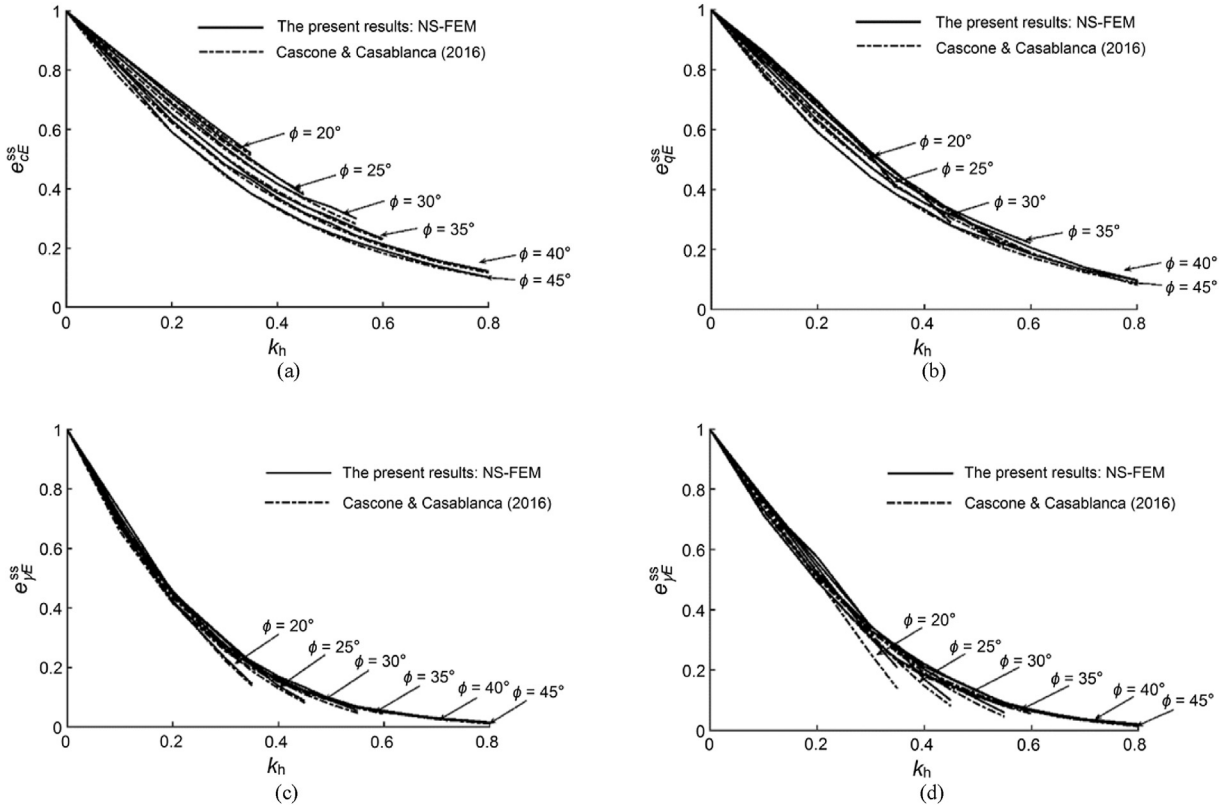

Fig. 14. Effect of superstructure horizontal acceleration k_h on the corrective coefficients: (a) e_{cE}^{ss}, (b) e_{qE}^{ss}, (c) $e_{\gamma E}^{ss}$ for smooth footing, and (d) $e_{\gamma E}^{ss}$ for rough footing.

Table 8
Variations in seismic bearing capacity factors with various combinations of k_h and k_v for $\varphi = 30°$.

k_h	k_v	N^s_{qE}	$N^s_{\gamma E}$ (smooth interface)	$N^s_{\gamma E}$ (rough interface)	N^{ss}_{cE}	N^{ss}_{qE}	$N^{ss}_{\gamma E}$ (smooth interface)	$N^{ss}_{\gamma E}$ (rough interface)
0	$k_v = 0$	18.63	7.68	14.97	30.44	18.63	7.68	15.57
	$k_v = 0.33k_h$	18.63	7.68	14.97	30.44	18.63	7.68	15.57
	$k_v = 0.5k_h$	18.63	7.68	14.97	30.44	18.63	7.68	15.57
	$k_v = k_h$	18.63	7.68	14.97	30.44	18.63	7.68	15.57
0.05	$k_v = -k_h$	19.15	8.05	14.39	27.03	16.48	6.26	12.9
	$k_v = -0.5k_h$	18.68	7.85	14.04	27.64	16.84	6.42	13.19
	$k_v = -0.33k_h$	18.52	7.79	13.92	27.85	16.97	6.47	13.29
	$k_v = 0$	18.21	7.66	13.69	28.27	17.23	6.53	13.51
	$k_v = 0.33k_h$	17.9	7.53	13.46	28.7	17.49	6.69	13.7
	$k_v = 0.5k_h$	17.74	7.47	13.34	28.92	17.63	6.75	13.81
	$k_v = k_h$	17.28	7.27	12.99	29.61	18.05	6.92	14.14
0.1	$k_v = -k_h$	19.59	8.37	15.05	23.77	14.47	4.98	10.98
	$k_v = -0.5k_h$	18.65	7.98	14.04	24.7	15.03	5.26	11.38
	$k_v = -0.33k_h$	18.33	7.85	13.8	25.02	15.23	5.37	11.53
	$k_v = 0$	17.71	7.59	13.45	25.69	15.63	5.58	11.81
	$k_v = 0.33k_h$	17.09	7.33	12.86	26.39	16.05	5.8	12.11
	$k_v = 0.5k_h$	16.77	7.2	12.62	26.76	16.28	5.92	12.27
	$k_v = k_h$	15.83	6.81	11.91	27.92	16.98	6.31	12.77
0.15	$k_v = -k_h$	19.99	8.65	15.13	21.03	12.78	3.67	9.51
	$k_v = -0.5k_h$	18.57	8.06	13.96	22.09	13.41	3.93	9.93
	$k_v = -0.33k_h$	18.09	7.86	13.59	22.47	13.64	4.03	10.07
	$k_v = 0$	17.15	7.47	12.85	23.24	14.10	4.33	10.37
	$k_v = 0.33k_h$	16.21	7.08	12.18	24.06	14.59	4.45	10.68
	$k_v = 0.5k_h$	15.73	6.88	11.81	24.5	14.85	4.57	10.84
	$k_v = k_h$	14.3	6.28	10.73	25.87	15.65	4.97	11.32
0.2	$k_v = -k_h$	20.34	8.9	15.27	18.71	11.33	3	8.25
	$k_v = -0.5k_h$	18.44	8.11	13.83	19.76	11.95	3.23	8.61
	$k_v = -0.33k_h$	17.79	7.83	13.34	20.14	12.16	3.31	8.74
	$k_v = 0$	16.53	7.31	12.31	20.88	12.59	3.47	8.97
	$k_v = 0.33k_h$	15.26	6.76	11.42	21.66	13.03	3.62	9.18
	$k_v = 0.5k_h$	14.6	6.49	10.92	22.06	13.25	3.7	9.28
	$k_v = k_h$	12.67	5.66	9.44	23.25	13.9	3.9	9.51
0.25	$k_v = -k_h$	20.66	9.13	15.47	16.71	10.07	2.67	6.44
	$k_v = -0.5k_h$	18.26	8.11	13.65	17.65	10.6	2.76	6.58
	$k_v = -0.33k_h$	17.44	7.76	13.03	17.97	10.78	2.82	6.62
	$k_v = 0$	15.84	7.08	11.67	18.6	11.12	2.92	6.91
	$k_v = 0.33k_h$	14.23	6.39	10.58	19.21	11.42	2.78	6.62
	$k_v = 0.5k_h$	13.4	6.02	9.94	19.5	11.53	2.68	6.56
	$k_v = k_h$	10.91	4.93	8.03	20.11	11.7	2.56	6.19
0.3	$k_v = -k_h$	20.94	9.32	15.61	14.97	8.98	2.02	5.51
	$k_v = -0.5k_h$	18.04	8.08	13.38	15.76	9.4	2.23	5.54
	$k_v = -0.33k_h$	17.04	7.65	12.62	16.02	9.52	2.25	5.51
	$k_v = 0$	15.09	6.8	10.98	16.47	9.69	2.25	5.4
	$k_v = 0.33k_h$	13.12	5.92	9.59	16.76	9.75	2.19	5.16
	$k_v = 0.5k_h$	12.09	5.46	8.78	16.86	9.75	2.11	4.97
	$k_v = k_h$	8.95	3.99	6.3	16.9	9.75	2.05	4.07
0.35	$k_v = -k_h$	21.2	9.49	15.74	13.48	8.04	1.26	4.75
	$k_v = -0.5k_h$	17.77	7.99	13.1	14.09	8.29	1.37	4.64
	$k_v = -0.33k_h$	16.59	7.48	12.18	14.24	8.34	1.43	4.55
	$k_v = 0$	14.27	6.45	10.21	14.46	8.36	1.66	4.29
	$k_v = 0.33k_h$	11.89	5.36	8.51	14.48	8.36	1.63	3.85
	$k_v = 0.5k_h$	10.63	4.76	7.5	14.48	8.36	1.6	3.54
	$k_v = k_h$	6.61	2.68	4.06	14.48	8.36	0.82	2.11
0.4	$k_v = -k_h$	21.63	9.64	15.84	12.19	7.21	1.19	4.1
	$k_v = -0.5k_h$	17.63	7.89	12.76	12.57	7.31	1.23	3.87
	$k_v = -0.33k_h$	16.24	7.27	11.69	12.64	7.31	1.23	3.73
	$k_v = 0$	13.48	6.05	9.34	12.67	7.31	1.19	3.57
	$k_v = 0.33k_h$	10.56	4.63	7.22	12.67	7.22	1.11	2.7
	$k_v = 0.5k_h$	8.93	3.83	5.88	12.67	7.02	0.95	2.28
	$k_v = k_h$	–	–	–	11.69	4.95	–	–
0.45	$k_v = -k_h$	21.84	9.76	15.91	11.05	6.48	1.11	3.56
	$k_v = -0.5k_h$	17.27	7.73	12.38	11.25	6.5	1.12	3.22
	$k_v = -0.33k_h$	15.66	6.99	11.13	11.26	6.5	1.06	3.03
	$k_v = 0$	12.34	5.47	8.32	11.26	6.45	0.92	2.74
	$k_v = 0.33k_h$	8.79	3.68	5.53	11.26	6.05	0.69	1.73
	$k_v = 0.5k_h$	6.46	2.33	3.07	10.97	5.55	0.44	1.2
	$k_v = k_h$	–	–	–	9.05	1.14	–	–
0.5	$k_v = -k_h$	22.03	9.86	15.95	10.05	5.85	1.03	3.09
	$k_v = -0.5k_h$	16.85	7.52	11.93	10.14	5.85	0.95	2.66
	$k_v = -0.33k_h$	15.01	6.66	10.47	10.14	5.85	0.8	2.44
	$k_v = 0$	11.16	4.76	7.18	10.14	5.62	0.68	2.02
	$k_v = 0.33k_h$	–	–	–	9.78	4.8	0.33	0.93
	$k_v = 0.5k_h$	–	–	–	9.35	3.96	–	–
	$k_v = k_h$	–	–	–	6.99	0.48	–	–

Table 8 (*continued*)

k_h	k_v	N^s_{qE}	$N^s_{\gamma E}$ (smooth interface)	$N^s_{\gamma E}$ (rough interface)	N^{ss}_{cE}	N^{ss}_{qE}	$N^{ss}_{\gamma E}$ (smooth interface)	$N^{ss}_{\gamma E}$ (rough interface)
0.55	$k_v = -k_h$	22.2	9.93	15.97	9.20	5.32	0.98	2.7
	$k_v = -0.5k_h$	16.36	7.26	11.4	9.22	5.32	0.89	2.2
	$k_v = -0.33k_h$	14.24	6.23	9.69	9.22	5.24	0.76	1.92
	$k_v = 0$	9.63	3.78	5.64	9.09	4.79	0.42	1.42
	$k_v = 0.33k_h$	–	–	–	8.46	3.52	–	–
	$k_v = 0.5k_h$	–	–	–	7.85	1.05	–	–
	$k_v = k_h$	–	–	–	5.06	0.3	–	–

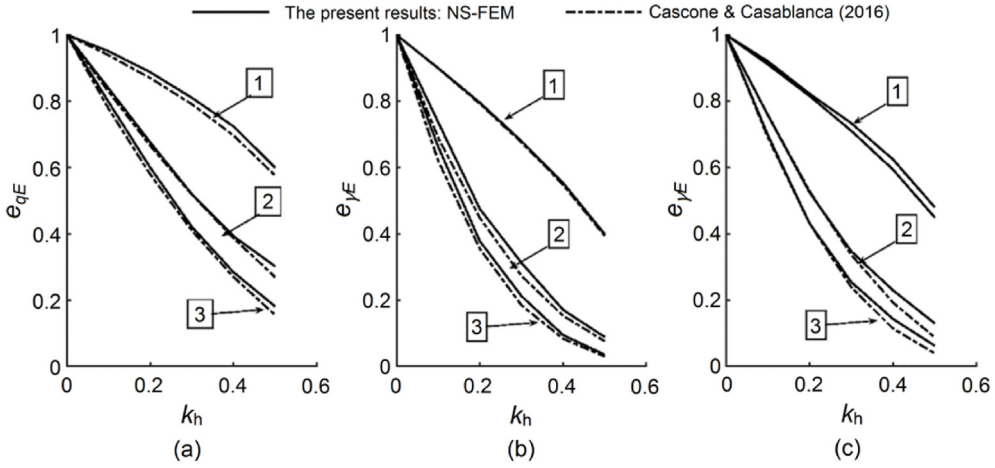

Fig. 15. The effect of soil and superstructure inertia on corrective coefficients in the case of $\phi = 30°$, $k_v = 0$, and $k_h = 0–0.5$: (a) e_{qE}, (b) $e_{\gamma E}$ for smooth footing, and (c) $e_{\gamma E}$ for rough footing. 1 – Effect of soil inertia; 2 – Effect of superstructure inertia; 3 – Effect of soil and superstructure inertia.

Table 9
Comparisons of the numerical results of N_{qE} with solutions available in literature ($\varphi = 30°$ and $k_v = 0$).

k_h	N_{qE}				e_{qE}			
	Buhdu and Al-Kani (1993)	Soubra (1999)	Cascone and Casablanca (2016)	Present method	Buhdu and Al-Kani (1993)	Soubra (1999)	Cascone and Casablanca (2016)	Present method
0	18.4	18.46	18.4	18.63	1	1	1	1
0.1	13.17	14.34	14.3	14.85	0.71	0.78	0.8	0.8
0.2	8.53	10.67	10.65	11.17	0.46	0.58	0.58	0.6
0.3	5.27	7.54	7.53	7.84	0.28	0.41	0.41	0.42
0.4	3.15	4.97	4.96	5.28	0.17	0.27	0.27	0.28
0.5	1.83	2.85	2.84	3.36	0.1	0.15	0.15	0.18

$$q_{ultE} = cN_{cE} + qN_{qE} + \frac{1}{2}\gamma BN_{\gamma E} \quad (17)$$

where $N_{cE} = N_c e^s_{cE} e^{ss}_{cE}$, $N_{qE} = N_q e^s_{qE} e^{ss}_{qE}$, and $N_{\gamma E} = N_\gamma e^s_{\gamma E} e^{ss}_{\gamma E}$, in which N_c, N_q and N_γ are the static bearing capacity factors.

Fig. 15 displays the variation of corrective coefficients for $\phi = 30°$, $k_v = 0$, and $k_h = 0–0.5$ for three cases: (i) the effect of soil inertia e^s_{qE} (curve 1), (ii) the effect of superstructure inertia e^{ss}_{qE} (curve 2), and (iii) the combined effect of soil and superstructure inertia e_{qE} (curve 3). The computational results indicate that the corrective coefficients e^s_{qE}, e^{ss}_{qE} and e_{qE} decrease continuously with increasing horizontal earthquake acceleration coefficient k_h. In general, the reduction of corrective coefficient e_{qE} is mainly due to the effect of superstructure inertia e^{ss}_{qE}. Furthermore, comparisons of N_{qE} and e_{qE} with previous studies in the case of $\phi = 30°$ and $k_v = 0$ are summarized in Table 9 and plotted in Fig. 16a and b, respectively. The corrective coefficient e_{qE} using NS-FEM is slightly higher than the Budhu and Al-Karni (1993) solution using the limit equilibrium method. In addition, the results of e_{qE} agree well with those from Soubra (1999) and Cascone and Casablanca (2016) using the limit equilibrium and the method of characteristics, respectively. It means that the seismic bearing capacity factor $N_{qE} = N_q e^s_{qE} e^{ss}_{qE}$ can be estimated by the superposition of the values of e^s_{qE} and $e^{ss}_{\gamma E}$.

Fig. 15b and c shows the influence of soil inertia (curve 1), superstructure inertia (curve 2) and combined effect (curve 3) on the corrective coefficients $e_{\gamma E}$ for smooth and rough foundations for $\phi = 30°$, $k_v = 0$, and $k_h = 0–0.5$. The values of $e^s_{\gamma E}$, $e^{ss}_{\gamma E}$ and $e_{\gamma E}$ decrease with an increasing horizontal earthquake acceleration coefficient k_h.

According to Fig. 15b and c, superstructure inertia $e^{ss}_{\gamma E}$ plays an important role in reducing corrective coefficients $e_{\gamma E}$ for smooth and rough interfaces. The obtained results of $N_{\gamma E}$ and $e_{\gamma E}$ for rough foundation are compared with solutions available in literature ($\phi = 30°$, and $k_v = 0$) in Table 10 and Fig. 16c and d. The coefficient $e_{\gamma E}$ for rough foundations agrees well with that reported by Cascone and Casablanca (2016), and the errors are within 5%. Moreover, most values of $e_{\gamma E}$ are slightly higher than those presented by Budhu and Al-Karni (1993), Soubra (1999) and Zhu

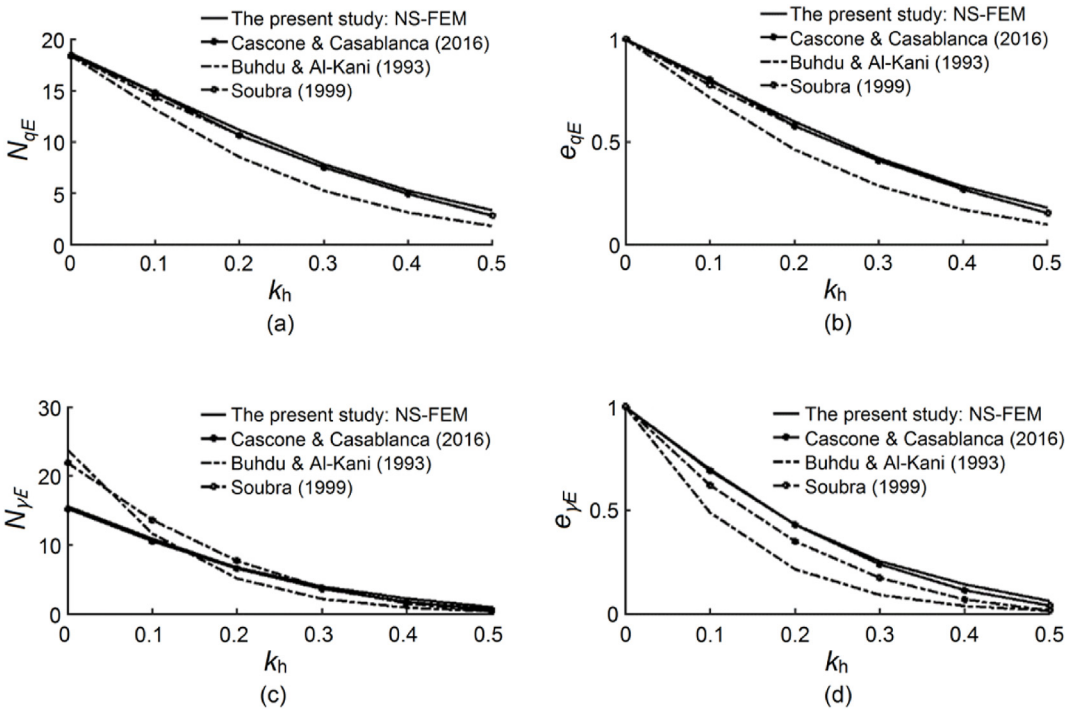

Fig. 16. Comparison of the present results with previous studies in the case of $\phi = 30°$, $k_v = 0$, and $k_h = 0–0.5$: (a) N_{qE}, (b) e_{qE}, (c) $N_{\gamma E}$ for rough footing, and (d) $e_{\gamma E}$ for rough footing.

Table 10
Comparisons of the numerical results of $N_{\gamma\ E}$ with solutions available in literature ($\phi = 30°$ and $k_v = 0$).

k_h	$N_{\gamma E}$ (rough footing)					$e_{\gamma E}$ (rough footing)				
	Budhu and Al-Karni (1993)	Soubra (1999)	Zhu (2000)	Cascone and Casablanca (2016)	Present method	Budhu and Al-Karni (1993)	Soubra (1999)	Zhu (2000)	Cascone and Casablanca (2016)	Present method
0	23.76	21.88	21.85	15.23	15.67	1	1	1	1	1
0.1	11.62	13.59	12.21	10.53	10.87	0.49	0.62	0.56	0.69	0.7
0.25	13	7.67	6.38	6.56	6.71	0.21	0.35	0.29	0.43	0.43
0.32	17	3.8	3.06	3.64	3.96	0.09	0.17	0.14	0.24	0.25
0.40	89	1.51	1.31	1.74	2.22	0.04	0.07	0.06	0.11	0.14
0.50	36	0.35	0.48	0.6	0.96	0.02	0.02	0.02	0.04	0.06

(2000) using different methods of analysis. The comparison confirms that the present study can give accurate values of the seismic bearing capacity factor $N_{\gamma E} = N_{\gamma} e^{s}_{\gamma E} e^{ss}_{\gamma E}$ using the superposition of the values $e^{s}_{\gamma E}$ and $e^{ss}_{\gamma E}$.

4. Conclusions

Using a pseudo-static approach, a NS-FEM was presented to estimate the static and seismic bearing capacities of shallow strip footings. A large number of simulations have been performed to study the bearing capacity of shallow strip footing under both static and seismic conditions, providing a new upper bound solution to all seismic bearing capacity components. Numerical results of both static and seismic bearing capacity factors are in good agreement with those using the slip-line method which correspond to the lower bound solutions to the bearing capacity. In addition, power dissipations obtained are identical to the slip-line networks given by Cascone and Casablanca (2016), providing knowledge of seismic effects on the failure mechanism of strip footing. Based on the numerical analyses, the following conclusions are made:

(1) In terms of the numerical procedure, combining the NS-FEM into the upper bound procedure can give accurate and reliable values of both static and seismic bearing capacity factors of shallow strip footing. The inclusion of horizontal and vertical seismic accelerations is presented in a straightforward and simple manner, providing an effective limit analysis to capture the ultimate load and the corresponding failure pattern under both static and seismic conditions.
(2) Separate calculations of all components of static and seismic bearing capacity factors to consider the effect of soil and superstructure inertia are performed and checked against the well-known Terzaghi's formula, with very satisfactory results.
(3) The numerical results reveal that the seismic bearing capacity depends on the direction of seismic acceleration in a highly complex manner. An upward vertical seismic acceleration results in a decrease in the magnitude of seismic bearing capacity. On the other hand, the vertical seismic acceleration in the downward direction causes a rise in the bearing capacity
(4) The corrective coefficients obtained show that superstructure inertia is a major contribution to reductions in the bearing capacity under seismic conditions compared with soil inertia. To facility practical applications, the superposition of both the soil inertia and the structure inertia has been presented to give safety values of seismic terms N_{cE}, N_{qE} and $N_{\gamma E}$.

(5) Variations of seismic bearing capacity with various combinations of seismic accelerations k_h and k_v are given in design tables and charts, providing useful knowledge of dependent seismic bearing capacity. These values can be used as references for engineers in the seismic design of a shallow foundation.

Declaration of competing interest

The authors declare that they have no known competing financial interests or personal relationships that could have appeared to influence the work reported in this paper.

Acknowledgments

This is part of the TPS project. The first author is grateful to a Vied-Newton PhD scholarship and a Dixon scholarship from Imperial College London, UK, for supporting his studies at Imperial College London. He is also indebted to the Dean's Fund from Imperial College London for financial support (2017–2020).

References

Abadie, C.N., 2015. Cyclic Lateral Loading of Monopile Foundations in Cohesionless Soils. PhD Thesis. University of Oxford, Oxford, UK.
Abadie, C.N., Houlsby, G.T., Byrne, B.W., 2019. A method for calibration of the hyperplastic accelerated ratcheting model (HARM). Comput. Geotech. 112, 370–385.
Ausilio, E., Conte, E., Dente, G., 2000. Seismic stability analysis of reinforced slopes. Soil Dynam. Earthq. Eng. 19 (3), 159–172.
Budhu, M., Al-Karni, A., 1993. Seismic bearing capacity of soils. Geotechnique 43 (1), 181–187.
Casablanca, O., Biondi, G., Cascone, E., Filippo, G.D., 2021. Static and seismic bearing capacity of shallow strip foundations on slopes. Geotechnique. https://doi.org/10.1680/jgeot.20.P.044.
Cascone, E., Casablanca, O., 2016. Static and seismic bearing capacity of shallow strip footings. Soil Dynam. Earthq. Eng. 84, 204–223.
Chakraborty, D., Kumar, J., 2013. Stability of a long unsupported circular tunnel in soils with seismic forces. Nat. Hazards 68 (2), 419–431.
Chen, J.S., Wu, C.T., Yoon, S., You, Y., 2001. A stabilized conforming nodal integration for Galerkin mesh-free methods. Int. J. Numer. Methods Eng. 50 (2), 435–466.
Choudhury, D., Subba Rao, K.S., 2005. Seismic bearing capacity of shallow strip footings. Geotech. Geol. Eng. 23, 403–418.
Ciria, H., Peraire, J., Bonet, J., 2008. Mesh adaptive computation of upper and lower bounds in limit analysis. Int. J. Numer. Methods Eng. 75 (8), 899–944.
Dormieux, L., Pecker, A., 1995. Seismic bearing capacity of foundation on cohesionless soil. J. Geotech. Eng. 121 (3), 300–303.
Ghosh, P., 2008. Upper bound solutions of bearing capacity of strip footings by pseudo-dynamic approach. Acta Geotech. 3, 115.
Hansen, J.B., 1970. A revised extended formula for bearing capacity. Dan. Geotech. Ins. Bull. (28), 5–11.
Hjiaj, M., Lyamin, A.V., Sloan, S.W., 2005. Numerical limit analysis solutions for the bearing capacity factor N_γ. Int. J. Solid Struct. 42 (5–6), 1681–1704.
Ho, P.L., Le, C.V., Chu, T.Q., 2019. The equilibrium cell-based smooth finite element method for shakedown analysis of structures. Int. J. Comput. Methods 16 (5), 1840013.
Houlsby, G.T., Abadie, C.N., Beuckelaers, W.J.A.P., Byrne, B.W., 2017. A model for nonlinear hysteretic and ratcheting behaviour. Int. J. Solid Struct. 120, 67–80.
Kalouzari, F.A., Izadi, A., Chenari, J.R., 2019. Seismic bearing capacity of shallow strip foundations in the vicinity of slopes using the lower bound finite element method. Soils Found. 59 (6), 1891–1905.
Krabbenhoft, K., 2018. Static and seismic earth pressure coefficients for vertical walls with horizontal backfill. Soil Dynam. Earthq. Eng. 104, 403–407.
Kumar, J., 2003. N_γ for rough strip footing using the method of characteristics. Can. Geotech. J. 40 (3), 669–674.
Kumar, J., Mohan Rao, V.B.K., 2003. Seismic bearing capacity of foundation on slopes. Geotechnique 53 (3), 347–361.
Le, C.V., 2017. Estimation of bearing capacity factors of cohesive-frictional soil using the cell-based smoothed finite element method. Comput. Geotech. 83, 178–183.
Le, C.V., Nguyen-Xuan, H., Askes, H., Bordas, S.P.A., Rabczuk, T., Nguyen-Vinh, H., 2010. A cell-based smoothed finite element method for kinematic limit analysis. Int. J. Numer. Methods Eng. 83 (12), 1651–1674.
Le, C.V., Nguyen-Xuan, H., Askes, H., Rabczuk, T., Nguyen-Thoi, T., 2013. Computation of limit load using edge-based smoothed finite element method and second-order cone programming. Int. J. Comput. Methods 10 (1), 1340004.
Liu, G.R., Dai, K.Y., Nguyen, T.T., 2007a. A smoothed finite element method for mechanics problems. Comput. Mech. 39 (6), 859–877.
Liu, G.R., Nguyen, T.T., Dai, K.Y., Lam, K.Y., 2007b. Theoretical aspects of the smoothed finite element method (SFEM). Int. J. Numer. Methods Eng. 71 (8), 902–930.
Liu, G.R., Nguyen-Thoi, T., Lam, K.Y., 2009a. An edge-based smoothed finite element method (ES-FEM) for static, free and forced vibration analyses of solids. J. Sound Vib. 320 (4–5), 1100–1130.
Liu, G.R., Nguyen-Thoi, T., Nguyen-Xuan, H.B., Lam, K.Y., 2009b. A node-based smoothed finite element method (NS-FEM) for upper bound solutions to solid mechanics problems. Comput. Struct. 87 (1–2), 14–26.
Makrodimopoulos, A., Martin, C.M., 2007. Upper bound limit analysis using simplex strain elements and second-order cone programming. Int. J. Numer. Anal. Methods GeoMech. 31 (6), 835–865.
Martin, C.M., 2005. Exact bearing capacity calculations using the method of characteristics. In: Barla, G., Barla, M. (Eds.), Proceedings of the 11th International Conference on Computer Methods and Advances in Geomechanics (IACMAG 05). Patron Editore, Bologna, Italy, pp. 441–450.
Meng, J., Zhang, X., Huang, J., Tang, H., Mattsson, H., Laue, J., 2020. A smoothed finite element method using second-order cone programming. Comput. Geotech. 123, 103547.
Meyerhof, G.G., 1951. The ultimate bearing capacity of foundation. Geotechnique 2 (4), 301–332.
Meyerhof, G.G., 1953. The bearing capacity of foundations under eccentric and inclined loads. In: Proceedings of the 3rd International Conference on Soil Mechanics and Foundation Engineering, vol. 1. Zürich, Switzerland, pp. 440–445.
Meyerhof, G.G., 1963. Some recent research on the bearing capacity of foundations. Can. Geotech. J. 1 (1), 16–26.
MOSEK ApS, 2009. The MOSEK Optimization Toolbox for MATLAB Manual, Version 5.0. MOSEK ApS, Copenhagen, Denmark.
Nguyen, H.C., 2020. Safety factor and failure mechanism in geotechnical engineering: a numerical study. In: Prashant, A., Sachan, A., Desai, C. (Eds.), Advances in Computer Methods and Geomechanics. Springer, Singapore, pp. 121–129.
Nguyen, H.C., 2021a. The use of adaptive smoothed finite-element limit analysis to seismic stability of tunnels. In: Elshafie, M.Z.E.B., Viggiani, G.M.B., Mair, R.J. (Eds.), Geotechnical Aspects of Underground Construction in Soft Ground. CRC Press, London, pp. 330–336.
Nguyen, H.C., 2021b. Upper bound analysis of seismic stability of tunnels using cell-based smoothed finite element. In: Elshafie, M., Viggiani, G., Mair, R. (Eds.), Geotechnical Aspects of Underground Construction in Soft Ground: Proceedings of the 10th International Symposium on Geotechnical Aspects of Underground Construction in Soft Ground (IS-Cambridge 2022). CRC Press, Boca Raton, USA, p. 337.
Nguyen, H.C., Vo-Minh, T., 2022. Calculation of seismic bearing capacity of shallow strip footings using the cell-based smoothed finite element. Acta Geotech. (in press).
Nguyen, H.C., Le, C.V., Nguyen, T.M., 2011. Estimation of bearing capacity and failure mechanism of strip footing using upper bound limit analysis. In: The 1st International Conference on Computational Science and Engineering. Ho-Chi-Minh City, Vietnam.
Nguyen-Xuan, H., Rabczuk, T., Nguyen-Thoi, T., Tran, T.N., Nguyen-Thanh, N., 2012. Computation of limit and shakedown loads using a node-based smoothed finite element method. Int. J. Numer. Methods Eng. 90 (3), 287–310.
Prandtl, L., 1920. Über die härte plastischer körper. Nachrichten von der Gesellschaft der Wissenschaften zu Göttingen. In: Mathematisch-Physikalische Klasse. Berlin Weidmannsche Buchhandlung, Berlin, Germany, pp. 74–85 (in German).
Reissner, H., 1924. Zumerddruck problem. In: Proceedings of the 1st International Congress of Applied Mechenics. Delft, The Netherlands, pp. 295–311.
Richards, R., Elms, D.G., Budhu, M., 1993. Seismic bearing capacity and settlements of foundations. J. Geotech. Eng. 119 (4), 662–674.
Saha, A., Ghosh, S., 2015. Pseudo-dynamics analysis for bearing capacity of foundation resting on c-φ soil. Int. J. Geotech. Eng. 9 (4), 379–387.
Saha, A., Saha, A.K., Ghosh, S., 2018. Pseudodynamics bearing capacity analysis of shallow strip footing using the advanced optimization technique "Hybrid symbiosis organisms search algorithm" with numerical validation. Adv. Civ. Eng. 2018, 3729360.
Sahoo, J.P., Kumar, J., 2012. Seismic stability of a long unsupported circular tunnel. Comput. Geotech. 44, 109–115.
Sahoo, J.P., Kumar, J., 2014. Stability of a circular tunnel in presence of pseudostatic seismic body forces. Tunn. Undergr. Space Technol. 42, 264–276.
Sarma, S.K., Iossifelis, I.S., 1990. Seismic bearing capacity factors of shallow strip footings. Geotechnique 40 (2), 265–273.
Sloan, S.W., Kleeman, P.W., 1995. Upper bound limit analysis using discontinuous velocity fields. Comput. Methods Appl. Mech. Eng. 127 (1–4), 293–314.
Soubra, A.H., 1999. Upper bound solutions for bearing capacity of foundations. J. Geotech. Geoenviron. Eng. 125 (1), 59–68.
Terzaghi, K., 1943. Theoretical Soil Mechanics. John Wiley & Son Inc;., New York, USA.
Tin-Loi, F., Ngo, N.S., 2003. Performance of the p-version finite element method for limit analysis. Int. J. Mech. Sci. 45 (6–7), 1149–1166.
Vesic, A.S., 1973. Analysis of ultimate loads of shallow foundations. J. Soil Mech. Found. Div., ASCE 99 (1), 45–73.
Vicente da Silva, M., Antao, A.N., 2007. A non-linear programming method approach for upper bound limit analysis. Int. J. Numer. Methods Eng. 72 (10), 1192–1218.
Vo-Minh, T., 2020. Calculation of bearing capacity factors of strip footing using the node-based smoothed finite element method (NS-FEM). In: Duc Long, P.,

Dung, N. (Eds.), Geotechnics for Sustainable Infrastructure Development. Springer, Singapore, pp. 1127–1134.
Vo-Minh, T., Nguyen-Son, L., 2021. A stable node-based smoothed finite element method for stability analysis of two circular tunnels at different depths in cohesive-frictional soils. Comput. Geotech. 129, 103865.
Vo-Minh, T., Nguyen-Minh, T., Chau-Ngoc, A., Nguyen-Chanh, H., 2017. Stability of twin circular tunnels in cohesive-frictional soil using the node-based smoothed finite element method (NS-FEM). J. Vibroeng. 19 (1), 520–538.
Vo-Minh, T., Chau-Ngoc, A., Nguyen-Minh, T., Nguyen-Chanh, H., 2018. A node-based smoothed finite element method for stability analysis of dual square tunnels in cohesive-frictional soils. Sci. Iran. 25 (3), 1105–1121.
Wang, L., Zhang, X., Tinti, S., 2021a. Large deformation dynamic analysis of progressive failure in layered clayey slopes under seismic loading using the particle finite element method. Acta Geotech. 16, 2435–2448.
Wang, L., Zhang, X., Zhang, S., Tinti, S., 2021b. A generalized Hellinger-Reissner variational principle and its PFEM formulation for dynamic analysis of saturated porous media. Comput. Geotech. 132, 103994.
Zhu, D., 2000. The least upper-bound solutions for bearing capacity factor N_γ. Soils Found. 40 (1), 123–129.

Dr. H.C. Nguyen obtained his PhD degree in Civil Engineering at Imperial College London, UK. During his PhD, Dr. Nguyen was awarded the Dean's Fund from Imperial College London (2017–2020). After his PhD studies, Dr. Nguyen worked as a postdoctoral research associate in Computational Geomechanics group at the University of Liverpool. He developed advanced numerical procedures using 3D SPFEM for large deformation analyses in geotechnical engineering.